




Protonation/deprotonation-driven switch for the redox stability of low-potential [4Fe-4S] ferredoxin

Reviewed Preprint

v1 • November 15, 2024

Not revised

Kei Wada , Kenji Kobayashi, Iori Era, Yusuke Isobe, Taigo Kamimura, Masaki Marukawa, Takayuki Nagae, Kazuki Honjo, Noriko Kaseda, Yumiko Motoyama, Kengo Inoue, Masakazu Sugishima, Katsuhiko Kusaka, Naomine Yano, Keiichi Fukuyama, Masaki Mishima, Yasutaka Kitagawa , Masaki Unno 

Department of Medical Sciences, University of Miyazaki, Kiyotake, Japan • Frontier Science Research Center, University of Miyazaki, Kiyotake, Japan • Graduate School of Science and Engineering, Ibaraki University, Hitachi, Japan • Graduate School of Engineering Science, Osaka University, Toyonaka, Japan • Department of Molecular Biophysics, Tokyo University of Pharmacy and Life Sciences, Tokyo, Japan • Department of Biochemistry and Applied Biosciences, Faculty of Agriculture, University of Miyazaki, Miyazaki, Japan • Department of Medical Biochemistry, Kurume University School of Medicine, Kurume, Japan • Comprehensive Research Organization for Science and Society (CROSS) Neutron Science and Technology Center, Naka Ibaraki, Japan • Graduate School of Science, Osaka University, Toyonaka, Japan • Structural Biology Division, Japan Synchrotron Radiation Research Institute, Hyogo, Japan • Research and Education Center for Atomic Sciences Ibaraki University, Naka Ibaraki, Japan

 https://en.wikipedia.org/wiki/Open_access

 Copyright information

eLife Assessment

Ferredoxins are ubiquitous electron transfer proteins that drive essential metabolic processes across all domains of life. This **fundamental** contribution to the field provides the first description of how specific amino acids, through a series of hydrogen bonds, control the ability of iron-sulfur clusters in ferredoxins to accept and donate electrons. The evidence supporting the conclusions is **compelling** as is the combined use of neutron crystallography with X-ray crystallography and classical spectral/redox studies.

<https://doi.org/10.7554/eLife.102506.1.sa2>

Abstract

Ferredoxin is a small iron-sulfur protein and acts as an electron carrier. Low-potential ferredoxins harbor [4Fe-4S] cluster(s), which play(s) a crucial role as the redox center. Low-potential ferredoxins are able to cover a wide range of redox potentials (–700 to –200 mV); however, the mechanisms underlying the factors which control the redox potential are still enigmatic. Here, we determined the neutron structure of ferredoxin from *Bacillus thermoproteolyticus*, and experimentally revealed the exact hydrogen-bonding network involving the [4Fe-4S] cluster. The density functional theory calculations based on the hydrogen-bonding network revealed that protonation states of the sidechain of Asp64 close to the [4Fe-4S] cluster critically affected the stability of the reduced state in the cluster. These

findings provide the first identification of the intrinsic control factor of redox potential for the [4Fe-4S] cluster in low-potential ferredoxins.

Introduction

Ferredoxin is known as a simple iron-sulfur (Fe-S) protein, and is ubiquitous in plants, animals, and prokaryotes(1 [↗](#), 2 [↗](#)). Ferredoxins function as electron carriers for fundamental metabolic processes such as gluconeogenesis/glycolysis, photosynthesis, nitrogen fixation, and assimilation of hydrogens and sulfur species. Therefore, ferredoxins have a variety of redox partners. In photosynthetic organisms, ferredoxin receives an electron from photosystem I complex and serves as the electron donor for the reduction of NADP^+ (ferredoxin: NADP^+ oxidoreductase), pyruvate (pyruvate:ferredoxin oxidoreductase), nitrate (nitrate reductase), and sulfite (sulfite reductase) to generate sources of energy(3 [↗](#)). In bacteria, oxidized ferredoxins are reduced *via* a reverse reaction such as by bacterial type ferredoxin: NADP^+ oxidoreductase and pyruvate:ferredoxin oxidoreductase, and electrons in the reduced ferredoxin are utilized by ferredoxin-dependent enzymes in various metabolism cascades(4 [↗](#)).

Typical bacterial ferredoxin is a small protein consisting of approximately one hundred amino acid residues, primarily (approximately 20%) negatively charged residues, with an isoelectric point (pI) that is usually below pH 4.0. The ferredoxin also has four conserved cysteine residues to which the Fe-S cluster is ligated in most cases. The types of the cluster are known as the [4Fe-4S] types(5 [↗](#)) (**Fig.1** [↗](#)). [4Fe-4S] ferredoxins may be further classified into low-potential and high-potential ferredoxins. Intriguingly, [4Fe-4S] ferredoxins exhibit a wide range of redox potentials while having the same form of the cluster in the active site(6 [↗](#)). For instance, low-potential ferredoxins harboring [4Fe-4S] exhibit redox potentials typically ranging from -700 mV to -200 mV; in contrast, high-potential ferredoxins have redox potentials of $+100$ mV to $+360$ mV(7 [↗](#)). Low-potential [4Fe-4S] ferredoxins, which are typical bacterial-type ferredoxins, reduce most of the redox partners at physiological potentials, whereas high-potential ferredoxins called HiPIPs usually accept electrons from most redox partners. Notably, electron transfer events by low-potential [4Fe-4S] ferredoxins are remarkable reactions; the low-potential ferredoxin receives an electron and must maintain the reduced [4Fe-4S] cluster until it transfers the electron to the redox partner proteins. How the low-potential [4Fe-4S] cluster maintains stability in the reduced form is unknown. The surrounding environment of the [4Fe-4S] cluster must be conferred and controls electron competency/stability; however, the mechanism underlying the sophisticated regulation of the redox potential and electron flow are still elusive.

Computer simulations using model complexes of the Fe-S cluster showed that the covalent nature of the Fe-S cluster decreases due to hydrogen bonds with the surrounding amino acid residues, and the redox potential correlates well with the covalent nature(8 [↗](#)). This indicates that the redox potential may be controlled by the hydrogen bonds between the main chain amide nitrogen and the sulfur in iron-sulfur clusters ($\text{NH}\cdots\text{S}$). In contrast, Solomon and co-workers demonstrated the substantial influence of hydration, supplied by water molecules, on the variation in reactivity by X-ray absorption spectroscopy(9 [↗](#)). The Fe-S covalency is much lower in natively hydrated [4Fe-4S] ferredoxin active sites but increases upon water removal. The density functional theory (DFT) calculations have supported a correlation between Fe-S covalency and ease of oxidation and therefore suggest that hydration accounts for most of the differences between ferredoxin redox potentials. However, the most critical problem in the computational calculations for the protein is that artificial coordinates for hydrogen atoms, which are predicted and generated computationally, have been used thus far for the calculations.

The precise locations of the hydrogen atoms in proteins are difficult to determine experimentally because this requires high-resolution structural information. So far, the exceptional ultra-high-resolution structure at 0.48 Å for HiPIP from *Thermochromatium tepidum* has been reported by X-

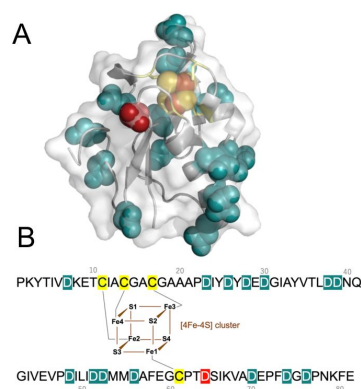


Fig. 1

Ternary and primary structures of low-potential [4Fe-4S] *BtFd*.

(A) The 3D structure of BtFd (PDB id: 1IQZ). The [4Fe-4S] cluster and aspartate residues are shown as a space-filling model, and the ligand cysteines for the Fe-S cluster are shown as yellow sticks. The surface drawing is superposed on the cartoon model. (B) Whole amino acid sequence of BtFd. The ligating manner of the [4Fe-4S] cluster is illustrated, and the ligand cysteine and aspartate residues are highlighted.

ray crystallography(10 [↗](#)), and the details of the hydrogen bonding networks surrounding the [4Fe-4S] cluster were determined. Using the charge-density analysis focused the valence electron, and the iron 3*d* and sulfur 3*p* electrons of the high-potential (positivity potential) [4Fe-4S] cluster were visualized for the first time. This is currently the most accurate analysis of the protein structure, but few indications regarding the stability of the redox state of the [4Fe-4S] cluster were obtained. More recently, the neutron structure of the HiPIP has been reported, indicating that the orientation of the amide proton of Cys75, one of the ligand residues for the Fe-S cluster, was probably altered in the reduced and oxidized states, possibly because of the electron storage capacity of the iron-sulfur cluster(11 [↗](#)).

The high-resolution structure of the low-potential [4Fe-4S] ferredoxin was reported using a gram-positive bacterium *Bacillus thermoproteolyticus* (*BtFd*). *BtFd* is a typical bacterial ferredoxin and is a small protein, a protein with pI in the acidic region, that consists of 81 residues and one [4Fe-4S] cluster (Fig. 1 [↗](#)). The X-ray structure of *BtFd* has been reported at a 0.92 Å resolution(12 [↗](#)), but the hydrogen atoms, particularly around the Fe-S clusters, could not be assigned on the electron density map. The DFT calculations, based on the *BtFd* structure, reported that the Fe-S covalencies of [4Fe-4S] clusters differ considerably from HiPIP because of hydrogen bonds with water molecules(9 [↗](#)). In this case, the hydrogen-bonding networks surrounding the Fe-S clusters also used the putative positions based on the calculations.

Neutron crystallography is a powerful analytic method because the hydrogen atoms can be visualized and the radiation damage is negligible. In this study, we proceeded to experimentally visualize the hydrogen bonds around the oxidized [4Fe-4S] cluster in *BtFd* by neutron crystal structure analysis under ambient air conditions and using the DFT method based on the experimentally determined hydrogen bonding network. The DFT calculations revealed that the protonation states of Asp64 located close to the reduced/oxidized [4Fe-4S] cluster significantly affected the redox stability of the cluster. Furthermore, the autooxidation kinetics of the reduced [4Fe-4S] cluster of *BtFd* prepared under anaerobic conditions supported the notion that Asp64 is critically involved in the stability of the reduced [4Fe-4S] cluster. These findings provide the first identification of intrinsic factors controlling the redox stability of the [4Fe-4S] cluster in low-potential ferredoxins.

Results

Overall neutron structure of the low-potential [4Fe-4S] ferredoxin

We have successfully determined the crystallization conditions of *BtFd* in which we could obtain large crystals (>2 mm³) using the dialysis method. The neutron structure of *BtFd* at room temperature was refined to a 1.60 Å resolution. The *R*-factor and free *R*-factor were 16.7% and 18.4%, respectively (Table 1 [↗](#)). A total of 819 H/D atoms and 60 hydrating water molecules were identified (Fig. 2A [↗](#), Table 1 [↗](#), and Fig. S1 [↗](#)). The overall structure was nearly identical to the previously reported cryogenic X-ray structure (PDB ID: 1IQG) at 0.92 Å resolution, with a rms deviation of 0.16 Å for Ca atoms when all residues (81 residues) were superimposed with least-squares fitting. Although the neutron-scattering length density map clearly shows the [4Fe-4S] cluster, the density for sulfur atoms was very low compared with most of the other atoms including the iron atoms (Fig. 2B [↗](#)). This is a reasonable result because the sulfur atom has a smaller neutron-scattering length *b_c* (10⁻¹² cm) (³²S=0.2804) than other atoms (⁵⁶Fe=0.994, ¹²C=0.6651, ¹⁴N=0.937, ¹⁶O=0.5803). The ability to clearly distinguish between iron atoms and sulfur atoms is one of the characteristics of neutron structure analysis. We also collected the X-ray diffraction data from the same crystal used for neutron diffraction intensity measurements, and the 1.45 Å resolution X-ray structure, obtained at room temperature, was also refined (Table 1 [↗](#)).

The electron density map of the [4Fe-4S] cluster showed the respective locations of iron and sulfur atoms with strong electron densities (**Fig. 2C**). Consequently, the joint refinement of the neutron structure with the X-ray structure gave the precise coordinates of the [4Fe-4S] cluster.

Hydrogen atoms around the low-potential [4Fe-4S] cluster

In the neutron structure, the hydrogen atoms around the [4Fe-4S] cluster were visualized, and the exact direction of hydrogen bonds could be determined (**Fig. 2D** and **E**). The Sy of cysteine residues, as ligands of the [4Fe-4S] cluster, formed five hydrogen bonds with the main chain amino groups; Cys11-Sy formed two hydrogen bonds with Ala13-NH and Ala33-NH, Cys14-Sy bonded to Ala16-NH, and Cys61-Sy bonded to Ile12-NH and Ser65-NH. In contrast, the Sy of Cys17 formed no hydrogen bond. The sulfur in the [4Fe-4S] cluster also formed hydrogen bonds; [4Fe-4S]-S1 with Gly15-NH and [4Fe-4S]-S3 with Ile12-NH. In addition, we observed the hydrogen atom of the water molecule (Water 237) close to the [4Fe-4S] cluster, which was bonded to [4Fe-4S]-S1 atom. In total, 9 hydrogen bonds were clearly identified around the [4Fe-4S] cluster (**Fig. 2E**). Nevertheless, the previously reported X-ray structure of [4Fe-4S] *BtFd* was at 0.92 Å resolution, and all of the hydrogen bonds were invisible. This demonstrated that neutron analysis is an indispensable method for determining the location of hydrogen atoms; the experimentally determined distances/angles are shown in **Fig. 2E**. Incidentally, depending on the bonding mode in which the S atom is bonded, if the S atom is a hydrogen bond acceptor, the -N-H...S hydrogen bond distance is estimated to be approximately 3.0 Å. In a special case known as a resonance-assisted H-bond, a -N-H...S distance of 2.44 Å has also been reported, in which case a strong hydrogen bond is formed(13). The average distance between the oxygen and the sulfur is reported to be 3.32 Å, and the distance of the nitrogen and sulfur is 10% longer compared to that of the oxygen and sulfur(13); the distance between the nitrogen and sulfur is estimated to be approximately 3.6–3.7 Å.

Importantly, the structural comparison showed that the neutron structure in this study was able to accurately revise the hydrogen network around the [4Fe-4S] cluster (**Fig. 2F**). The -OH group on the sidechain of Thr63 was located an appropriate distance from the [4Fe-4S] cluster in order to form a hydrogen bond. This group was thought to be hydrogen-bonded in previous X-ray study(12) as the hydrogen atom in this position was not visible, but the distance as well as the angle between the donor and acceptor atoms indicated the possibility of the formation of a sulfur-containing hydrogen bond(14). In the neutron crystal structure, Thr63-Oy1 and the [4Fe-4S]-S4 atoms were also within the hydrogen-bonding distance (3.5 Å), however, the hydrogen atom identified pointed in a different direction from the iron-sulfur cluster, indicating that it did not form a hydrogen-bonding interaction with the iron-sulfur cluster (**Fig. 2F**). Furthermore, the neutron-scattering length density clearly revealed hydrogen bonding to another residue; the sidechain of Thr63-Oy1H and the main chain -CO of Thr10 clearly formed a hydrogen bond at a distance of 2.2 Å. In order to consider the redox potential, it is important to experimentally determine the exact hydrogen-bonding network, and, ultimately, a single hydrogen bond can make a critical difference.

Density functional theory calculations of the low-potential [4Fe-4S] cluster in *BtFd*

In this study, we were able to revise the hydrogen-bonding network around the low-potential [4Fe-4S] cluster. We then investigated the effect of hydrogen bonding around the active site by the DFT calculations using the [4Fe-4S] cluster model based on the neutron diffraction structure including some amino acid residues (**CM**), as shown in **Fig. 3A**. The Cartesian coordinates of the model are summarized in **Table S1**. At first, the charge/spin state of each iron atom in the [4Fe-4S] cluster was examined using a cluster model without amino acid (**CM_{NA}**) as shown in **Fig. 3A**. In accordance with previous reports(15, 16), the total energies of the 12 possible combinations of charge/spin alignments were examined for the [Fe^{III}₂Fe^{II}₂] (oxidized: Ox) and [Fe^{III}Fe^{II}₃]

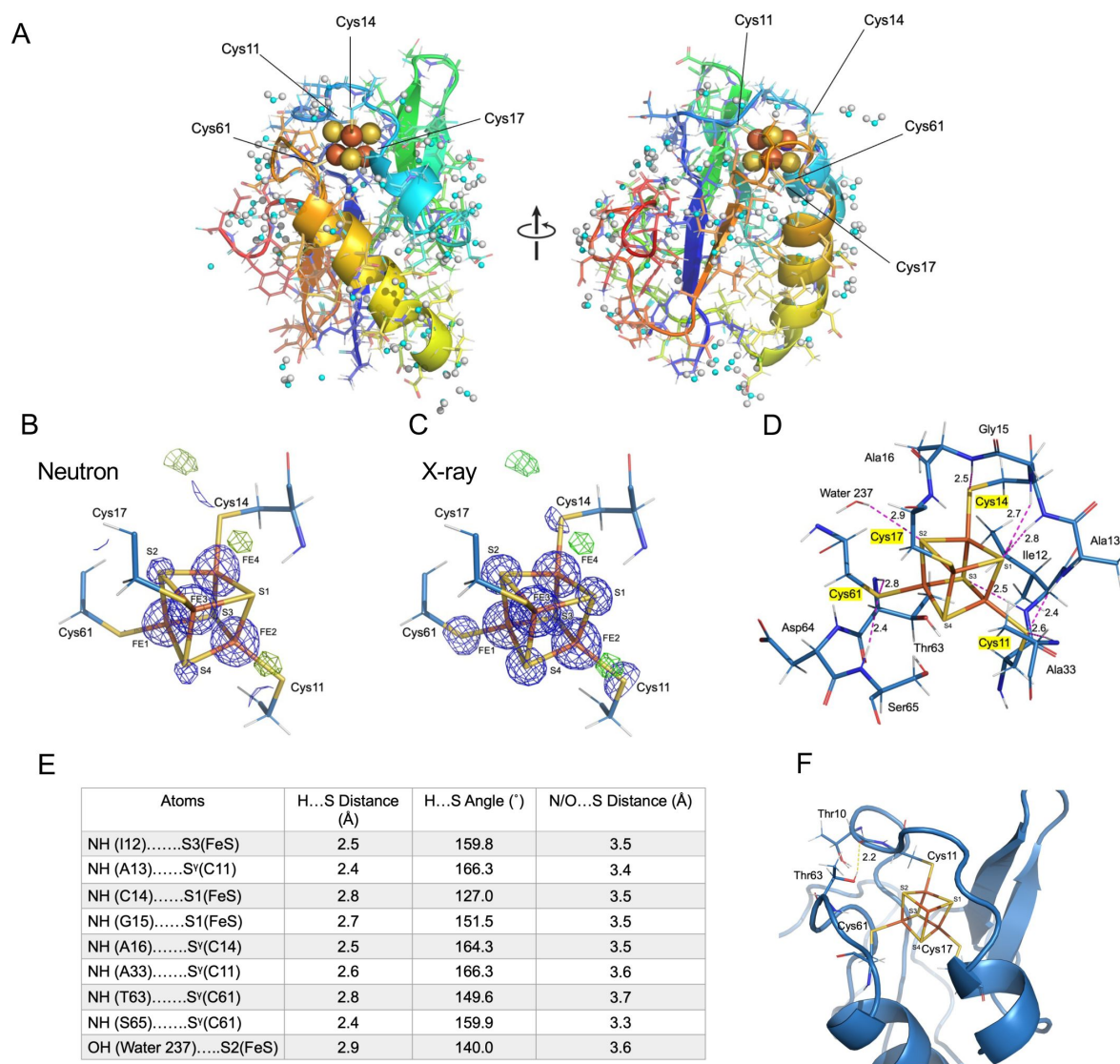


Fig. 2

Neutron structure of low-potential [4Fe-4S] BtFd

(A) Overall neutron structure of BtFd. BtFd polypeptides are colored in rainbow colors from blue (N-terminus) to red (C-terminus). The [4Fe-4S] cluster and water molecules are shown as a space-filling model. White and cyan balls indicate hydrogen (deuterium) and oxygen atoms, respectively. The figure on the right is the left one rotated approximately 90°. (B) The $2F_o - F_c$ (1.0 sigma: blue cage) and $F_o - F_c$ (3.0 sigma: green cage) neutron-scattering length density map around the [4Fe-4S] cluster and the structural model. The $2F_o - F_c$ map is shown within 1 Å around the [4Fe-4S] cluster for clarity. (C) X-ray electron density map of the corresponding region of (B). $2F_o - F_c$ (5.0 sigma) and $F_o - F_c$ (3.0 sigma) maps are shown in blue and green, respectively. (D) Hydrogen bond with the [4Fe-4S] cluster and its ligand Sy atoms of cysteines. The hydrogen (deuterium), oxygen, carbon, and nitrogen atoms are shown in white, red, cyan, and blue, respectively. The hydrogen bonds indicate pink broken lines and the distance between the amide hydrogen and sulfur atoms is shown in angstroms. (E) The distances and angles of the hydrogen bonds. The distance/angle between the hydrogen and the sulfur are shown on the left and the center columns, and the distance between nitrogen/oxygen and sulfur are shown on the right column. (F) Hydrogen bond between Thr63-OH and the main chain -CO of Thr10.

Data Collection		
	Neutron	X-ray
Beamline	iBIX at MLF in J-PARC	NW12A at PF-AR
Wavelength (Å)	1.5 – 4.5	1.0000
Exposure time	6 hours/1 set	0.5 second/0.5°
Number of datasets (neutron) or images (X-ray)	58 (15 days)	720
Transmittance (%)	100	5
Resolution (Å)	15.12 – 1.60 (1.69 – 1.60)	50.00 – 1.45 (1.48 – 1.45)
Space group	C2	
Cell parameters (Å, °)	$a = 70.5, b = 37.9, c = 33.0$ $\beta = 106.0$	
Multiplicity	7.5 (6.2)	6.7 (6.1)
Completeness (%)	94.2 (76.8)	100 (100)
R_{merge}	0.137 (0.369)	0.080 (0.553)
$I/\sigma(I)$	12.9 (4.9)	25.2 (2.5)
Joint refinement		
$R_{\text{work}}/R_{\text{free}}$	0.167/0.184	0.147/0.159
<i>r.m.s</i> Bond lengths (Å)	0.010	–
<i>r.m.s</i> Bond angles (°)	1.067	–
Total No. of hydrogen atom	598	–
Total No. of deuterium atom	221	–
No. of H atoms in protein	598	–
No. of D atoms in protein	110	–
No. of H atoms in water	0	–
No. of D atoms in water	111	–

Table 1.

Statistics for Neutron and X-ray Diffraction Data

(reduced: *Red*) states as summarized in [Table S2](#). As shown in [Fig. 3B](#), the most stable spin alignments for the *Ox* and *Red* states are confirmed to be consistent with the states previously reported([16](#)), thus we assumed those charge/spin alignments in the following calculations. Next, to estimate the effect of hydrogen bonding, the vertical ionization potential (IP) was estimated by the calculated energy gaps between oxidized [*E*(*Ox*)] and reduced [*E*(*Red*)] states([16](#), [17](#)).

The calculated IP value of **CM** was -3.27 eV, suggesting the *Ox* state was 3.27 eV more stable than the *Red* state in this structure. In order to consider the effect of the surrounding amino acids, the IP value was also calculated using **CM_{NA}**. The calculated IP value was -4.15 eV, which was shifted 0.88 eV to the negative side in comparison with **CM**, suggesting that the surrounding amino acids affect the IP value. In the previous study([18](#)), it was reported that [N–H \cdots S] hydrogen bonds involved with the cluster stabilize the reduced state and shift the IP of the cluster to the positive side. Our result was, therefore, consistent with the previous study([18](#)). However, a single [N–H \cdots S] hydrogen bond is suggested to change the IP value approximately 0.3 eV([18](#)), so the 0.88 eV shift was much smaller than the value expected from the neutron structure (9 hydrogen bonds) around the active site. To explain this underestimation in the IP value, the lowest unoccupied molecular orbital (LUMO) of the oxidized state, which was the corresponding orbital in this redox reaction, was examined as illustrated in [Fig. 3C](#). The LUMO was mainly localized around the 4Fe-4S cluster; however, unexpectedly appeared at the deprotonated Asp64. This means that the electron density is partially removed not only from the [4Fe-4S] cluster but also from Asp64 in the oxidation process (*Red* \rightarrow *Ox*). We note that the carboxy group of Asp64 is not neutralized ($-\text{COO}^-$) in the neutron structure, but it is easily protonated and neutralized since Asp64 is on the surface of the protein. Therefore, the IP of the cluster was recalculated with the **CM_H** model as illustrated in [Fig. 3A](#). Then the population of LUMO around Asp64 was removed and fully localized on the [4Fe-4S] cluster as illustrated in [Fig. 3C](#). Interestingly, the calculated IP of **CM_H** (-1.06 eV) was largely shifted to the positive side in comparison with the deprotonated **CM**. The difference in the IP value between **CM_H** and **CM_{NA}** (3.09 eV) indicates a contribution of 0.34 eV per one hydrogen bond, which is comparable to the previous report([18](#)). These results suggest that the protonation state of the sidechain of Asp64 plays important roles for the stability of the reduced state, and furthermore in the control of electron transfer. To examine the charge difference between **CM** and **CM_H** in the simulation, we also constructed a new model including an additional OH^- ion around Asp64 (**CM_{HOH}**) as illustrated in [Fig. S2A](#). The total charge of the **CM_{HOH}** model corresponds to the **CM** model and includes the effect of the hydrogen bond. The calculated IP for the **CM_{HOH}** is -2.93 eV, therefore a contribution of a single hydrogen bond is 0.33 eV. This indicates that the relative stability of the *Red* state is suppressed compared with the **CM_H** but is significantly larger than the **CM**, suggesting the importance of the protonation of Asp64 ([Fig. S2B](#)).

To consider the effect of the structural change caused by the redox on the IP, geometrical optimization of the 4Fe-4S core was performed for the **CM** and **CM_H** models using the same level of theory to the single-point calculations. The optimized Cartesian coordinates are summarized in [Table S3](#). As illustrated in [Fig. S2A](#), the IP values of **CM** and **CM_H** change from -3.27 to -2.38 eV ($|\Delta\text{IP}| = 0.89$ eV), and from -1.06 to -0.19 eV ($|\Delta\text{IP}| = 0.87$ eV), respectively. These results indicate that the IP values are significantly affected by the structural rearrangement; however, the shifts ($|\Delta\text{IP}|$) are the same between the **CM** and **CM_H** models. In other words, the effect of the structural change on the redox in the IP value is important but the significance of the protonation to Asp64 is not changed, regardless of the structural rearrangement.

To consider the environmental effect of the surrounding protein, we also introduced The Polarizable Continuum Model (PCM) using the Integral Equation Formalism variant (IEFPCM) approximation. As summarized in [Table S4](#) in detail, IP values of **CM** and **CM_H** becomes 1.62 eV and 2.59 eV, respectively, indicating that the environmental effect significantly changes the IP value. On the other hand, a qualitative relationship between the IP values of the **CM** and **CM_H** models is not changed, although the difference in the IP values between **CM** and **CM_H** (IP) is

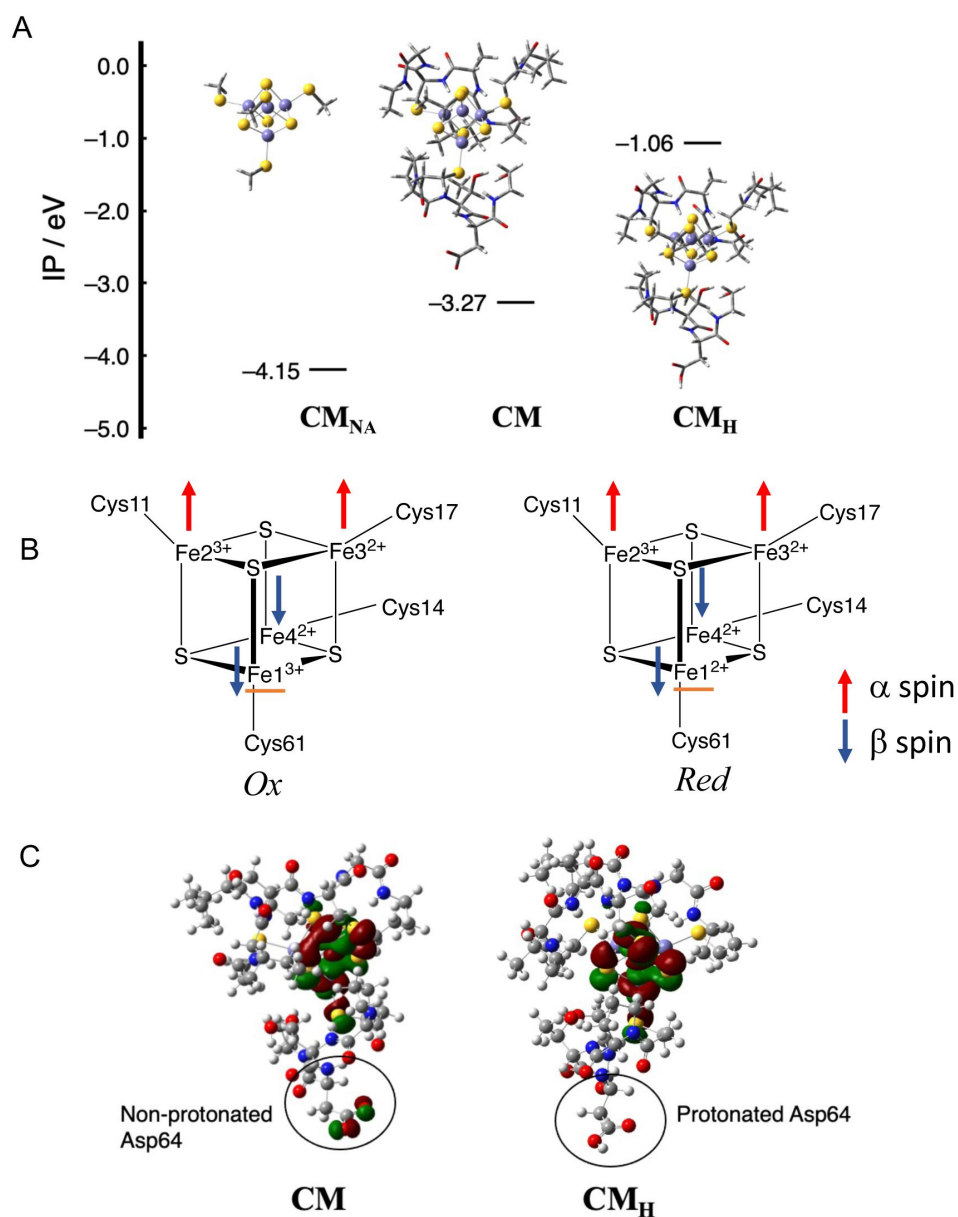


Fig. 3

DFT calculation based on the neutron structure of [4Fe-4S] *BtFd*

(A) Illustration of model structures (CM_{N} , CM , and CM_{H}) and their calculated *IP* values. (B) Assumed charge/spin states of the [4Fe-4S] cluster for Ox and Red states. Fe1 is indicated by the orange underscore and dominantly changes its charge state. (C) Distribution of LUMOs of CM and CM_{H} . The red and green colors indicate positive and negative phases, respectively.

decreased from ca. 2.2 to 1.0 eV. From these results, we can conclude that the protein environment is essential for their IP values but does not change the relative difference between **CM** and **CM_H** (IP) qualitatively.

The role of Asp64 in *BtFd* for the air-oxidation of the low-potential [4Fe-4S] cluster

The DFT calculations highlighted the influence of the Asp64 protonation state on the IP value of the [4Fe-4S] cluster. The IP value is directly reflected in the oxidation rate of the [4Fe-4S] cluster in atmospheric air, since the electron transfer rate to oxygen depends on the IP. In *BtFd*, the ultraviolet-visible (UV-Vis) spectra were changed between reduced and oxidized states of the [4Fe-4S] cluster (**Fig. 4A**); the absorption shoulders around 320 nm and 420 nm were increased by oxidation. Therefore, we prepared reduced *BtFd* under anaerobic conditions and measured the spectral changes at 420 nm, associated with air oxidation.

In wild-type *BtFd*, the time-dependent change of the UV-Vis spectrum is associated with oxidation of the [4Fe-4S] cluster and displayed typical Michaelis-Menten kinetics (**Fig. 4B**). Therefore, we applied the global fitting to evaluate the oxidation rate (half time of maximum oxidation ($T_{1/2}$) as for the K_m in substrate affinity), and in the evaluation, small numbers indicated the fast oxidation reaction. Multiple measurements of the oxidation rates showed a $T_{1/2}$ of 100 sec for wild-type *BtFd*. In contrast, that of D64A-mutated *BtFd* was 166 sec, approximately 1.7 times slower than wild type. The D64N mutant also had a slow oxidation rate at 170 sec. These results clearly indicate that a neutralizing mutation in Asp64 leads to a slow oxidation rate, and the reduced state of the [4Fe-4S] cluster has greater stability than that of wild type.

BtFd has 15 aspartate residues including Asp64, all of which are located in the solvent-exposed environment (**Fig. 1**). We mutated each aspartate to alanine and evaluated changes in oxidation rates; however, only mutations in Asp64 resulted in oxidation rate changes (**Fig. 4B** and **Fig. S3**). *BtFd* also has 5 glutamate residues, but none of these affected the oxidation rate (**Fig. S3**).

More interestingly, the D64N neutralizing mutation had the same effect on [4Fe-4S] as the D64A mutation, and the D64R mutation, a positively charged mutant, also slowed the similar oxidation rate (**Fig. 4B**). In contrast, the D64E mutation, a negatively charged mutation, did not affect the oxidation rate. Namely, the carboxy group in this position exposed to solvent is indispensable for the function of the electron transfer.

The role of Asp64 in low-potential [4Fe-4S] *BtFd* for the redox potential

To further evaluate the effect of the mutation, we determined the redox potential (E° , V versus standard hydrogen electrode (SHE), pH 7.0 of each mutant by the cyclic voltammetry method; **Fig. 4C**). As a result, the redox potential of wild-type *BtFd* was estimated to be -346 mV. In contrast, the potentials of the D64A and D64N-mutated *BtFd* were -276 mV and -286 mV, respectively. The potential of the D64E mutation was -346 mV, similar to that of the wild type. The neutralizing mutation in the Asp64 position causes the positive shift of 60 ~ 70 mV in redox potential. The potential of the D64R mutation was estimated to be -307 mV, but its deviation is large (± 41.6 mV).

The effect of aspartate/glutamate residue in various ferredoxins harboring the low-potential [4Fe-4S] cluster

We performed further experiments to confirm whether the results obtained with *BtFd* are the same for various ferredoxins from different organisms. We attempted to overexpress and purify eight ferredoxins as in the phylogenetic tree (**Fig. 5A**) from Eukaryote, Archaea, and Bacteria, in which three of them were successfully obtained from the ferredoxins harboring the [4Fe-4S] or

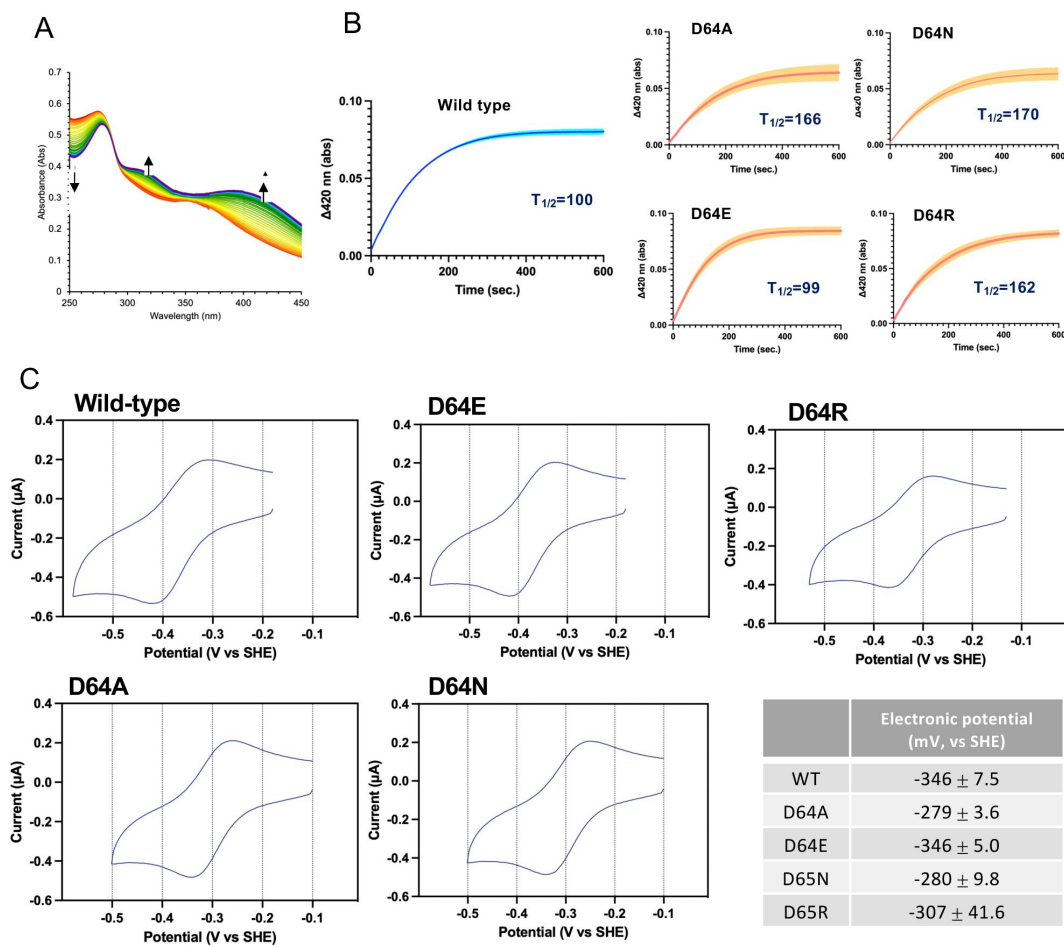


Fig. 4

Spectral changes upon [4Fe-4S] cluster oxidation and typical voltammogram of *BtFd* and its mutant proteins

(A) Time-dependent changing of UV-vis absorption spectrum of wild-type *BtFd* by air oxidation. The spectra are colored in rainbow colors from red (reduced *BtFd*) to purple (oxidized *BtFd*). The arrows indicate the absorbance increase at 340 nm, 420 nm, and indicate the absorbance decrease at 260 nm. (B) The absorption changes of the Asp64 mutated *BtFds* at 420 nm recorded every second. The standard deviations calculated from at least 3 times the measurements indicated as the line width with the light color. The $T_{1/2}$ value (sec) is indicated in the inset. (C) The cyclic voltammograms obtained at the disposable screen-printed carbon electrode from a solution of as isolated 100 μM *BtFd* or its mutated proteins in 50 mM Tris-HCl (pH 7.0), 150 mM NaCl and 2.5 mM neomycin, at sweep rate of 50 mV/s. The CV measurement performed in the anoxic chamber ($O_2 < 5$ ppm).

[3Fe-4S] cluster. The [4Fe-4S] ferredoxin from *Staphylococcus haemolyticus*, a close relative to *Bacillus thermoproteolyticus*, has an aspartate residue at the position of 65 (**Fig. S4C**), which corresponds to Asp64 in *BtFd*. The measurement of the air-oxidation rate indicated that the Asp65 mutation critically affected the rate as seen in that of *BtFd* (**Fig. 5B**). In the *Megalodesulfobacterium* (*Desulfovibrio*) *gigas* [3Fe-4S] ferredoxin, the Glu53 is the corresponding position to the Asp64 in *BtFd* (**Fig. S4C**). The air-oxidation rate is quite slow and its rate is further slowed by introducing the E53A mutation (**Fig. 5B**). Surprisingly, even in the archaeal *Geoglobus acetivorans* [4Fe-4S] ferredoxin, which is phylogenetically quite distant from *BtFd*, the E56A mutation affected the oxidation rate (**Fig. 5B**).

Discussion

Redox potentials are major contributors to controlling electron transfer rates and thus regulating electron transfer processes in biological reactions. Elucidating how proteins control the redox potentials of Fe-S clusters is a longstanding fundamental question. Possible controlling factors that have been proposed as being important include the solvent exposure of the cluster, specific hydrogen-bonding networks, especially NH...S bonds, and the proximity and orientation of the protein backbone and sidechain dipoles.^(7, 19–22) Thus far, several mutagenesis studies have demonstrated that the redox potential of ferredoxin can be changed by introducing artificial mutations into residues near Fe-S clusters. For instance, in [4Fe-4S] ferredoxin from *Azotobacter vinelandii* (AvFd I), mutations in positions Phe2 or Phe25 showed a large shift (100–200 mV versus SHE) in reduction potentials⁽²³⁾. The series of mutations based on the sequence/structural comparison among AvFd I and *Peptostreptococcus asaccharolyticus* ferredoxin (PaFd) and related ferredoxins showed that three mutations, V19E, P47S, and L44S in AvFd I also shift to higher reduction potentials (130 mV increasing in total)⁽¹⁹⁾. These artificial mutation studies clearly showed the significance of the environment of [4Fe-4S] for redox potentials; however, their intrinsic control residues have remained ambiguous.

In this study, we showed that Asp64 in the *BtFd* affected the behaviors of the [4Fe-4S] cluster including the redox potential (**Fig. 4B** and **C**). During the course of the purification, all of the mutated *BtFd* eluted at the same conductivity from the high-resolution ion-exchange column, that is, the aspartate mutation in various positions did not disturb the net charge of this protein. Also, the respective UV-Vis spectra of the reduced and oxidized forms of *BtFd* mutants were the same as that of the wild type (**Fig. S4**), demonstrating that the environment of the [4Fe-4S] cluster was not altered by these mutations. These results indicated that the acidic residue mutations in other positions did not significantly affect the oxidation rate (**Fig. 4B**). The distances between the Asp/Glu and [4Fe-4S] cluster are listed in **Table S5**; the sidechain of Asp64 is located at 10.1 Å, and the Asp7 (10.5 Å), Asp26 (12.0 Å), Asp28 (11.3 Å), Asp30 (13.7 Å), Asp53 (13.7 Å), Glu9 (13.7 Å), and Glu59 (12.8 Å) were located at similar distances. Taken together, only Asp64 affects the oxidation rate of the [4Fe-4S] cluster, and the protonation state of Asp64 directly contributes to the control of electron potential of the [4Fe-4S] cluster.

The mutation experiments showed that the Asp64 residue in *BtFd* was exchangeable with a glutamate residue, which means that the carboxy group in this position is indispensable. The sequence alignment of the low-potential [4Fe-4S] ferredoxin demonstrated that negatively charged residues, aspartate or glutamate, are highly conserved at this position among low-potential [4Fe-4S] ferredoxins in bacteria (**Fig. S6**). Interestingly, the significance of the highly conserved aspartate or glutamate was demonstrated for the ferredoxins from different organisms even in organisms distantly related in the evolutionary phylogenetic tree (**Fig. 5A** and **B**). That is, the effect of the D64A mutation in the [4Fe-4S] *BtFd* in gram-positive bacteria is also observed in the E56A mutation and in archaeal [4Fe-4S] ferredoxin from *Geoglobus acetivorans*. Furthermore, the

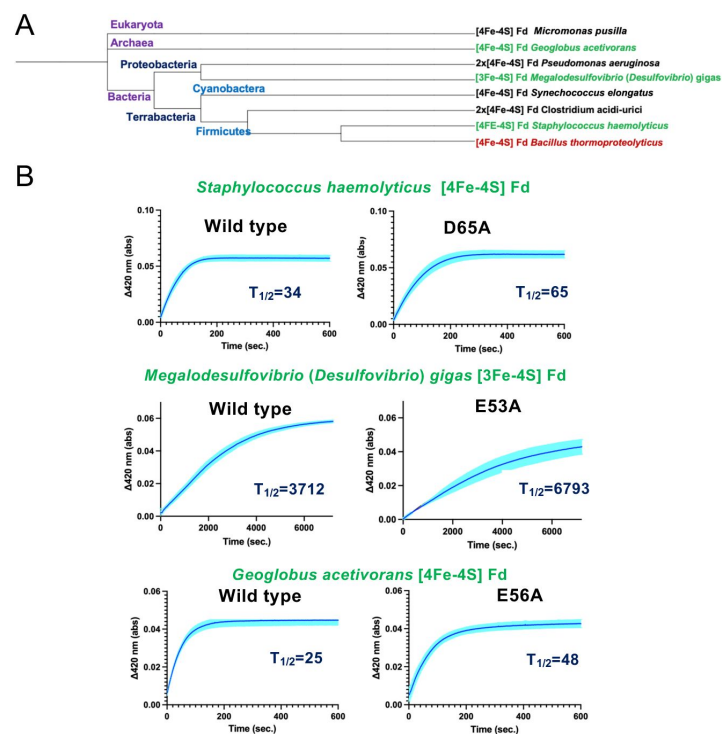


Fig. 5

The effect of aspartate/glutamate residue in various ferredoxins harboring the low-potential [4Fe-4S] cluster

(A) Phylogenetic tree of ferredoxin harboring the [4Fe-4S], [4Fe-4S] x 2 and [3Fe-4S] cluster from various organism. (B) The air-oxidation absorption changes at 420 nm of various ferredoxin and its Asp/Glu mutated ferredoxin are also indicated.

same results are obtained from the [4Fe-3S] ferredoxin from *Megalodesulfobrevibacter gigas*, a gram-negative bacterium. Thus, the control mechanism of the redox-state stability found in *BtFd* may be a common mechanism, at least in low-potential [4Fe-4S] and [3Fe-4S] ferredoxins.

In general, the pKa value of the aspartic acid sidechain is a pH of approximately 3.9, meaning that under physiological conditions, the sidechain of Asp64 is constantly in a deprotonated state. We have attempted to determine the pKa value of the Asp64 in *BtFd* by monitoring the chemical shifts of the Asp64 sidechain $^{13}\text{CO}(\gamma)$ using nuclear magnetic resonance to determine the pH titration of Asp64. Under the reduced conditions we could not determine the pKa value of the carboxylate hampering the paramagnetic property of the reduced [4Fe-4S] cluster. Instead, under the oxidative conditions (normal ambient air conditions), the pKa of Asp64 was successfully estimated to be approximately 4.9 (**Fig. S7A** and **B**, SI method and text). This indicated that the pKa of Asp64 shifted to neutral. To further estimate the pKa under reduced conditions, we applied the air-oxidation measurement; the oxidation rate of the wild-type *BtFd* changed dramatically between pH 6.0 to 7.0 (**Fig. S7C**). In contrast the D64A *BtFd* did not alter the rate according to the pH. These results indicate that the pKa value of Asp64 is thought to be between a pH of 6.0 to 7.0. The [4Fe-4S] cluster in the *BtFd* was stable enough to conduct these experiments under acidic to basic conditions (pH 4.5–9.0) (**Fig. S8**). Thus, the protonation/deprotonation of Asp64 likely occurs even in physiological conditions.

The structural basis of the interactions between ferredoxin and its partner proteins has been previously reported (24–26). In the reported structures, ferredoxins bound to their partner proteins such as ferredoxin:NADP⁺ oxidoreductase or photosystem I were required to directly face the Fe-S cluster region to effectively accept electrons from their partner proteins. These complex structures are derived from photosynthetic organisms, and ferredoxins harboring a [2Fe-2S] cluster are called plant-type ferredoxins. Unfortunately, there is no structural report about the characteristics of the interaction between bacterial [4Fe-4S] ferredoxins and their partner proteins, although the major interaction region of ferredoxin must be in close contact with the Fe-S cluster. In bacterial low-potential [4Fe-4S] ferredoxins, if an aspartate residue neighboring the [4Fe-4S] cluster, corresponding to Asp64 in *BtFd*, was protonated by complex formation, electrons received from the bacterial ferredoxin:NADP⁺ oxidoreductase complex are able to remain stable. According to the Frank-Condon principle, known as the ground rule of the electron transfer, the electronic transitions are relatively instantaneous compared with the time scale of nuclear motions. As well, in *BtFd*, the distance between the [4Fe-4S] cluster and the carboxy sidechain of Asp64 was close enough to enable the electron transfer as the corresponding distance is approximately 10 Å (**Table S5**). Therefore, the protonation state of the aspartate residue neighboring the [4Fe-4S]/[3Fe-4S] cluster is a reasonable switch to control the stability of the reduced state in the [4Fe-4S]/[3Fe-4S] cluster. We propose a control mechanism of the redox potential in low-potential [4Fe-4S]/[3Fe-4S] ferredoxins as shown in **Fig. S9**. This protonation-driven switch is likely reasonable to prevent the backflow of accepted electrons.

To our knowledge, this is the first proposed mechanism of the intrinsic control factor of redox potentials of the [4Fe-4S]/[3Fe-4S] cluster in low-potential ferredoxins. We hope that the determination of complex structures with electron donors and acceptors involving ferredoxin will elucidate more detailed control mechanisms for electron transfer by low-potential [4Fe-4S]/[3Fe-4S] ferredoxins.

Materials and Methods

Expression and purification of the low-potential ferredoxin of [4Fe-4S] *BtFd*

Expression and purification of [4Fe-4S] *BtFd* were conducted as previously reported(12, 27), with some modifications. The plasmid pET-21a(+)-*btfD* gene was co-expressed with the *isc* operon (pRK-ISC)(28) in the *E. coli* strain C41(DE3) to produce holo-*BtFd* in high yield. The bacteria were cultivated in 2.5 liters of Terrific broth containing 100 µg/mL ampicillin, 5 µg/mL tetracycline, and 0.1 mg/mL ferric ammonium citrate. Expression was induced with 0.5 mM IPTG and the cells were further grown for 20 h at 28°C. The cells were disrupted by sonication, and the suspension was centrifuged at 12,000 *g* for 30 min at 4°C. The colored supernatant was subjected to ammonium sulfate fractionation at 60% saturation. After centrifugation, the supernatant fraction was applied to HiPrep Butyl FF 16/10 (Cytiva, Marlborough, MA, USA) and eluted with a linear gradient of ammonium sulfate (5–25%) in 50 mM Tris-HCl, pH 7.8. The grayish brown fractions were dialyzed against a solution containing 50 mM Tris-HCl, pH 7.8, applied to an anion exchange column (Mono Q HR 5/5, Cytiva) chromatography using the NGC Quest 10 system (Bio-Rad Laboratories, Inc. Hercules, CA).

Expression and purification of the low-potential ferredoxin of [4Fe-4S], [4Fe-4S]₂, and [3Fe-4S] ferredoxin from various organisms

Expressions and purifications of [4Fe-4S] ferredoxins were conducted using the same procedures as that of *BtFd*. Each ferredoxin gene was constructed using a synthetic oligonucleotide (Eurofins Japan, Tokyo) based on UniProt database sequence optimized for the *E. coli* codon usage.

Crystallization of [4Fe-4Fe] *BtFd* for neutron crystallography

The crystallization procedure and conditions are as follows and were modified from the method reported previously to grow large crystals for neutron crystallography(12). Purified [4Fe-4S] *BtFd* was concentrated by centrifugation using an Amicon Ultra centrifugal filter unit 3K (Merck Millipore) to 30–40 mg/mL. The crystal for the neutron diffraction experiment was obtained with the dialysis method at 4°C using a 50 µL dialysis button (Hampton Research, Journey Aliso Viejo, CA, USA) and the excess amount of the reservoir solution containing 200 mM NaCl, 1.4 M ammonium sulfate, and 50 mM MES (pH 5.9). The crystal appeared within one month and was grown to approximately 2.5 mm × 1.8 mm × 0.6 mm in a month.

Neutron diffraction experiment

The crystal was soaked to 50 µL of 50 mM MES buffer (pD 6.3) containing 200 mM NaCl and 1.4 M ammonium-d8 sulfate (D8, 98%; Cambridge Isotope Laboratories Inc.) prior to the neutron diffraction experiment. The soaking solution was exchanged three times in three weeks. The crystal was mounted in a quartz glass capillary with 3.5 mm φ and 0.01 mm thickness (Hilgenberg). Inside the capillary, a small amount of deuterated reservoir solution was contained to avoid drying up the crystal, and the capillary was sealed with epoxy resin. Time-of-flight (TOF) neutron diffraction data were collected at BL03 iBIX (29) in a Japan Proton Accelerator Research Complex (J-PARC, Tokai, Japan) at room temperature. Thirty-two wavelength-shifting fiber-based scintillator neutron detectors with a surface area of 133 mm × 133 mm were used to collect the data. A total of 56 data sets were collected using a wavelength of 1.5–4.5 Å with a detector distance of 490 mm. Exposure time for each data set was 6 h at 500 kW of the J-PARC accelerator power. The TOF neutron data were indexed, integrated, scaled, and processed with STARGazer(30). The neutron diffraction data statistics are listed in Table 1.

X-ray diffraction experiment

X-ray diffraction data from the same crystal used for neutron crystallography were collected using an ADSC Quantum270 CCD detector at NW12A in Photon Factory Advanced Ring (PF-AR; Tsukuba, Japan) under room temperature. The wavelength of the synchrotron radiation, transmittance, and slit size were 1.000 Å, 1%, and 0.20 mm (horizontal) × 0.05 mm (vertical), respectively.³¹ The sample-to-detector distance, oscillation range and exposure time were 75 mm, 0.5° and 0.5 sec, respectively. In total, 720 images were collected. Data were integrated, merged, and processed with HKL-2000(31 [↗](#)). The X-ray diffraction data collection and statistics are listed in **Table 1** [↗](#).

Structure refinement

The structure was determined by molecular replacement method using the previously determined X-ray structure of [4Fe-4S] BtFd (PDB ID: 1IQZ) from which the waters and [4Fe-4S] cluster were removed as the initial model. The first refinement was carried out using the rigid-body refinement program RefMac5(32 [↗](#)) from 8.0 to 3.0 Å resolution range using only X-ray intensity data. The *R* factor was dramatically dropped by rigid-body refinement. Then, the joint refinement was carried out with both the neutron and X-ray diffraction data using PHENIX(33 [↗](#)). The 1.6 Å resolution neutron data and the 1.45 Å resolution X-ray data were used for the structure refinement. Five percent of the data were selected by PHENIX for cross-validation. The neutron scattering length density and electron density maps were visualized and manual model refinement was carried out using COOT(34 [↗](#)). Protonation states of amino acid residues and orientation of water molecules were manually adjusted by watching both the neutron scattering length density and electron density calculated before including the hydrogens (H)/deuteriums (D) on COOT; only the neutron scattering length density appeared for the positions of the H (negative density)/D (positive density) atoms. The temperature factors for all atoms and occupancies for H/D atoms and residues having dual conformations were also refined. The refinement statistics are also listed in **Table 1** [↗](#). All structure illustrations in figures except for **Fig. 3** [↗](#) were prepared with Pymol(35 [↗](#)).

DFT calculations

All calculations were performed by using the spin-unrestricted hybrid DFT method with the B3LYP functional set. As the basis set, 6-31G* and 6-31+G* were used for [Fe, C, N, O, H] and [S] atoms, respectively, for the IP calculations. Only the position of a hydrogen atom bound to a carboxy group of Asp64 in CM_H was optimized using the 6-31G [Fe, C, H], 6-31G* [N, O], and 6-31+G* [S] basis sets while the other atoms remained fixed. All of these calculations were carried out in gas phase conditions using the Gaussian 09 program package(36 [↗](#)).

The IP was defined as the vertical ionization potential values of the reduced state calculated by $IP = E(Ox) - E(Red)$, where $E(Ox)$ and $E(Red)$ were calculated as total energies of the oxidized (*Ox*) and reduced (*Red*) states by the DFT method(16 [↗](#), 17 [↗](#)).

Cartesian coordinates of calculated models are summarized in **Table S1** [↗](#). From the formal charges of Fe, S and other ligands, we assumed that the total charges of the CM_{NA} and CM models are −3 and −4 for oxidized (*Ox*) and reduced (*Red*) states, respectively, whilst total charges are −2 and −3 for the *Ox* and *Red* models in the case of the CM_H model. The CM_{HOH} model is constructed by placing the OH[−] ion close to Asp64 in the initial structure, followed by a geometric optimization of only the OH[−] fragment for both the reduced and oxidized states. To examine the effect of the OH[−] in detail, the OH[−] fragment is moved along the O–H axis of the OH[−] fragment in 0.5Å step. The spin states of *Ox* and *Red* states are the open-shell singlet and doublet states, respectively. The calculated Mulliken charges and spin densities of [4Fe-4S] cores are added in **Table S2** [↗](#). As mentioned in the main text, the most stable spin/charge alignment of Fe ions were examined among 12 possible spin/charge combinations using CM model, and all other following calculations were only assumed to be these ground states (see **Table S2A** [↗](#) and **B** [↗](#)). It is reported that the

molecular charges sometimes cause the error especially under approximation of the solvation effect by PCM(37), however the simulation is performed in the gas phase, therefore such effect is assumed to be negligible.

Oxidation rate analysis of [4Fe-4S] *BtFd* and its mutated proteins

Site-directed mutagenesis was carried out using a KOD-plus-Mutagenesis Kit (Toyobo), with a pET21a(+)-containing *BtFd* gene as a template. Sequence analysis verified that the resultant constructs were free of errors. Expression and purification of mutated [4Fe-4S] *BtFds* were performed in the same way as that for wild type. Prior to the oxidation rate measurement, we performed a complete reduction of [4Fe-4S] *BtFd* by using dithionite; 1 mM (final concentration) dithionite was added to 100 μ L of [4Fe-4S] *BtFd* (6.0 mg/ml) in anaerobic conditions ($O_2 < 5$ ppm; COY). After 1 h of incubation at 4 $^{\circ}$ C, the dithionite was removed by size-exclusion chromatography (HiTrap Desalting 5 ml column; Cytiva) equipped with the AKTA START system under anaerobic conditions. Complete removal of the dithionite was able to be confirmed with the chromatogram, which indicated the two separated peaks derived from the reduced [4Fe-4S] *BtFd* and dithionite. The fraction containing reduced [4Fe-4S] *BtFd* (1 mL) was moved into quartz cells with the screwcap under anaerobic conditions, and taken out of the anaerobic chamber. Then, the UV-Vis spectroscopic measurement (V730BIO, JASCO) was started immediately after the screwcap was opened. The spectral changes at 420 nm were measured every second for 10 mins, and the measurements were performed three times, at least for the global fitting. The temperature of the cell chamber in the spectrometer was strictly controlled at 28 $^{\circ}$ C by the Peltier water-cooled cell-holder and the cell solution was continuously mixed by a micro-stirrer. The global fittings of the Michaelis-Menten curve were performed using the kinetics curve fitting mode in the GraphPad Prism 9 (GraphPad Software, San Diego, CA USA, www.graphpad.com).

The electrochemical measurement of [4Fe-4S] *BtFd* and its mutated proteins

To exchange the buffer, the purified *BtFd* and its mutated proteins were precipitated by ammonium sulfate and the precipitate was suspended in the buffer at various pHs; the sample solutions contained 100 μ M *BtFd*, 625 mM NaCl, 2.5 mM neomycin, and 50 mM Tris-HCl at a pH of 7.8 or 50 mM MES-Tris mixed buffer at a pH of 6.0–9.0. The cyclic voltammetry was performed using the μ Stat-I 400 bipotentiostat (Metrohm AG, Switzerland) controlled by Drop-View 8400 software. A disposable screen-printed carbon electrode (DRP-110, Metrohm AG) was formed by a carbon ink and acted as a working electrode (4 mm diameter). Voltammetric measurements used Ag as a pseudo-reference electrode and carbon ink as a counter electrode. Five cyclic scans were recorded between -0.80 and -0.40 V at a 0.05 V s^{-1} sweep rate. The CV measurements were performed anaerobically by setting the devices, including the potentiostat and the disposable electrode, in an anaerobic chamber ($O_2 < 5$ ppm; COY).

Data availability

The atomic coordinates and structure factors for the neutron structure of the *BtFd* at room temperature have been deposited in the PDB under accession code 7YL8.

Acknowledgements

We would like to express our deepest appreciation to Research Fellows Ms. Makiko Ishihara and Dr. Kenji Ite for their many suggestions and advice. We thank Dr. Yu Hirano of the Institute for Quantum Life Science for the helpful advice on the neutron crystal structure analysis. We also

thank members of iBIX at J-PARC of Japan for the neutron diffraction data collection. The neutron diffraction experiments, including the test experiments, were conducted under Proposals 2016PX0003, 2017PX0004, 2019PX3020, and 2020PX3006 (Ibaraki Prefecture Project) in J-PARC. We thank members of the Structural Biology beamlines of PF and SPring-8 for the X-ray diffraction data collection, including preliminary experiments. The X-ray diffraction experiments were conducted under Proposals 2017G561 and 2019G512 in PF and 2022A2724 in SPring-8. This work was partly supported by JSPS KAKENHI numbers 23K17981 (to K.W.), 21H5260 (to K.W.), 20H03196 (to K.W.), 16K07261 (to M.U.), 21K05016 (to S.M.), 22H02562 (to M.M.), 21H01951 (to Y.K.), 22H02050 (to Y.K.), Ibaraki Prefecture's Sendokenkyu from 2016 to 2021 (to M.U.), The Takeda Science Foundation (to K.W.) and the Japan Foundation for Applied Enzymology (to K.W.). This research was partially supported by Research Support Project for Life Science and Drug Discovery (Basis for Supporting Innovative Drug Discovery and Life Science Research (BINDS)) from AMED and the Frontier Science Research Center, University of Miyazaki. We also thank T. Yokoyama, T. Kawaguchi, A. Yoshida and Y. Kawagoe of the University of Miyazaki for technical assistance.

Additional information

Author contributions

K.F., K.W. and M.U. initiated and directed this study together with Y.K., M.M. K.W., K.K. Y.I. and M.M. prepared proteins. K.K., Y.I., K.K., N.Y. and M.U. performed neutron and/or X-ray structural biology experiments. I.E., T.K. and Y.K. performed computational studies of the DFT calculations. M.M., K.I., M.S., K.F. and K.W. performed the biological experiments. All authors participate in the data analysis and manuscript preparation.

Competing interests

The authors declare no competing interest.

Supplementary Text

pKa estimation of Asp64 in BtFd by NMR spectroscopy

The stable isotopically labeled BtFd proteins were expressed in a 2 L M9 minimal medium containing 0.5 g/L $^{15}\text{NH}_4\text{Cl}$, with 4 g/L of unlabeled glucose, 1 g/L of $^{13}\text{C}_6$ -glucose for ^{15}N , or $^{13}\text{C}/^{15}\text{N}$ labeled as sole nitrogen and carbon sources, respectively. After induction, the cultures were incubated overnight at 25 °C, and the cells were harvested by centrifugation. The purification was performed in the same manner to the crystallization. The NMR sample for standard heteronuclear experiments was dissolved in 50 mM K-phosphate buffer (pH 6.9) containing 50 mM KCl and 7% D_2O . The final concentrations of BtFd in the samples were 0.9–1.5 mM in a final volume of 300 mL. Microcell NMR tubes (Shigemi) were used. All NMR spectra were processed with the software package NMRPipe (1) and analyzed using Sparky (2). All NMR experiments were performed at 303 K on a Bruker AVANCEIII(HD)600 instrument equipped with a TCI CRYOPROBE. As a first step for analyzing the pKa of the aspartate sidechains, we established the resonance assignments by standard heteronuclear multidimensional NMR technique (3). The backbone resonance assignments were obtained from the following two- and three-dimensional experiments: 2D ^1H - ^{15}N HSQC, 3D HNCO, HN(CA)CO, CBCA(CO)NH, and HNCACB. The sidechain aliphatic ^1H and ^{13}C assignments were obtained from the following three- and four-dimensional experiments: 3D C(CO)NH, 3D H(CCO)NH, 3D HCCH-TOCSY, and 4D HC(CO)NH (4). Based on the obtained aliphatic assignments, the $^{13}\text{CO(g)}$ resonance assignments of the aspartate sidechains were made by linking the adjacent $^{13}\text{C}\beta$ chemical shifts. Since the CO signals in the 1D ^{13}C experiment were heavily overlapped, we used the 2D CACO experiment (5) in which the ^{13}Ca offset of indirect dimension

was shifted to $^{13}\text{C}\beta$ (45 ppm) for monitoring the titrated signals. Namely, we diverted a CACO experiment originally used for correlations of backbone C α and CO to the sidechain CO assignment. To avoid the signal splitting caused by ^{13}C - ^{13}C spin coupling during ^{13}CO acquisition, low-bash homonuclear decoupling (6 [6](#)) was achieved in the experiments. The pH 3.5 buffer was composed of 50 mM phosphate and 50 mM KCl, the pH 4.0–5.0 buffer was composed of 50 mM acetate and 50 mM KCl, the pH 5.5–6.5 buffer was composed of 50 mM MES and 50 mM KCl, the pH 7.0–8.0 buffer was composed of 50 mM HEPES and 50 mM KCl, and the pH 8.5–9.0 buffer was composed of CHES and 50 mM KCl. These buffers contained 7% D $_2$ O for the lock signal. The pKa(s) were estimated from the Hill equation by nonlinear least-square curve fitting using Microsoft Excel implemented SOLVER module (Microsoft).

BtFd was stable enough to conduct the NMR experiments under acidic to basic conditions (pH 3.5–9.0), thus, we were able to estimate the pKa of aspartate sidechains by monitoring the chemical shifts of $^{13}\text{CO}(\gamma)$ (**Fig. S7A** [6](#)). Notably, $^{13}\text{CO}(\gamma)$ resonance of Asp64 is isolated from the others, and showed remarkable chemical shift changes upon pH titration (**Fig. S7** [6](#), **A** [6](#) and **B** [6](#)). The sigmoidal curve was obtained from the Asp64 signals and the pKa was estimated to be 4.9 (**Fig. S7B** [6](#)). The pKa value of Asp74 was also able to be estimated to be 5.0, although its chemical shift change was smaller than that of Asp64. The pKa values of the other residues were not able to be evaluated, since they showed no sigmoidal curves in the pH range of 3.5–9.0, or their signals were not reliably assigned. Interestingly, the pKa value of Asp74 was also shifted to a natural pH (**Fig. S7B** [6](#)). This Asp74 is located away from the [4Fe-4S] cluster at a distance of 22.4 Å (**Table S5** [6](#)), and the distance between Asp64 and Asp74 is approximately 10.1 Å. The function of Asp74 is unclear at this stage.

Fig. S1.

Neutron-scattering length density maps of [4Fe-4S] ferredoxins.

The $F_o - F_c$ neutron-scattering length density maps for the hydrogen/deuterium at 2.0σ contour levels. The pink and green cages represent the $+(F_o - F_c)$ and $-(F_o - F_c)$ map, respectively, and the final model of *BtFd* is superposed on the maps. The maps clearly indicate that the densities derived from the deuterium and hydrogen atoms are clearly visible in the neutron crystallography.

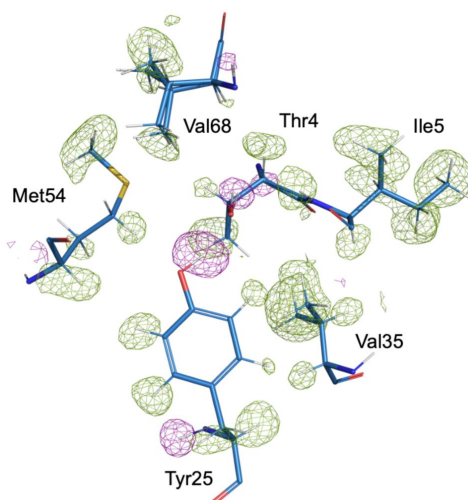
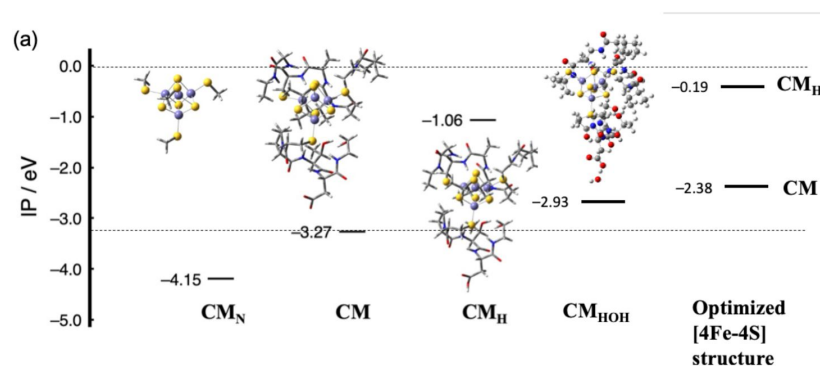


Fig. S2.

DFT calculation based on the neutron structure of [4Fe-4S] BtFd. Calculated IP values of each model.



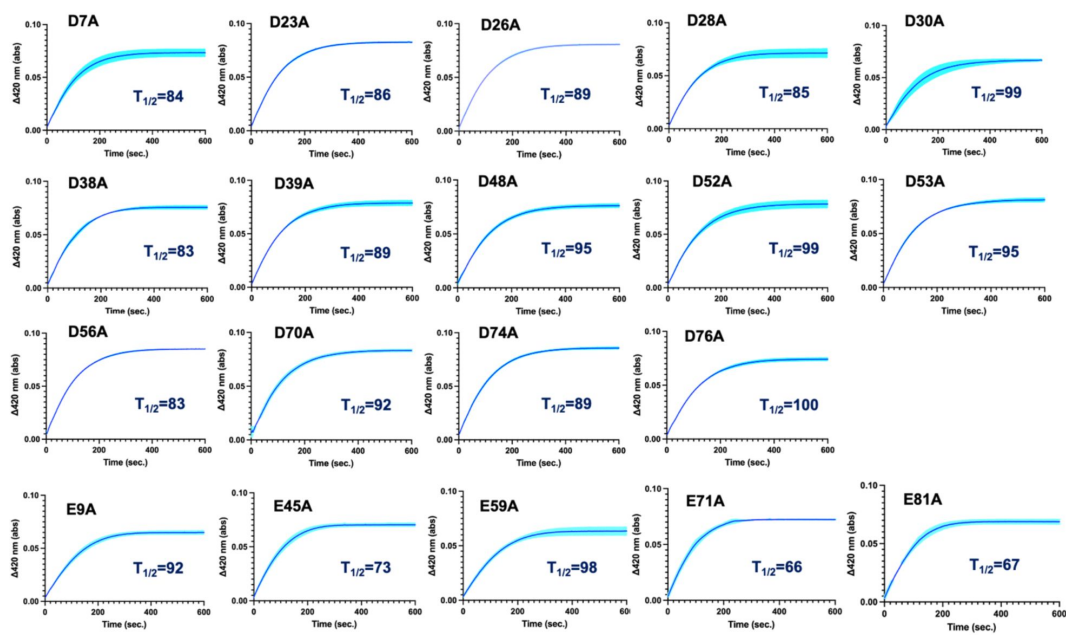


Fig. S3.

The absorption changes of various mutated *BtFds* at 420 nm recorded every second.

The standard deviations calculated from at least 3 times the measurements indicated as the line width with the light color. The $T_{1/2}$ value (sec) is indicated in the inset.

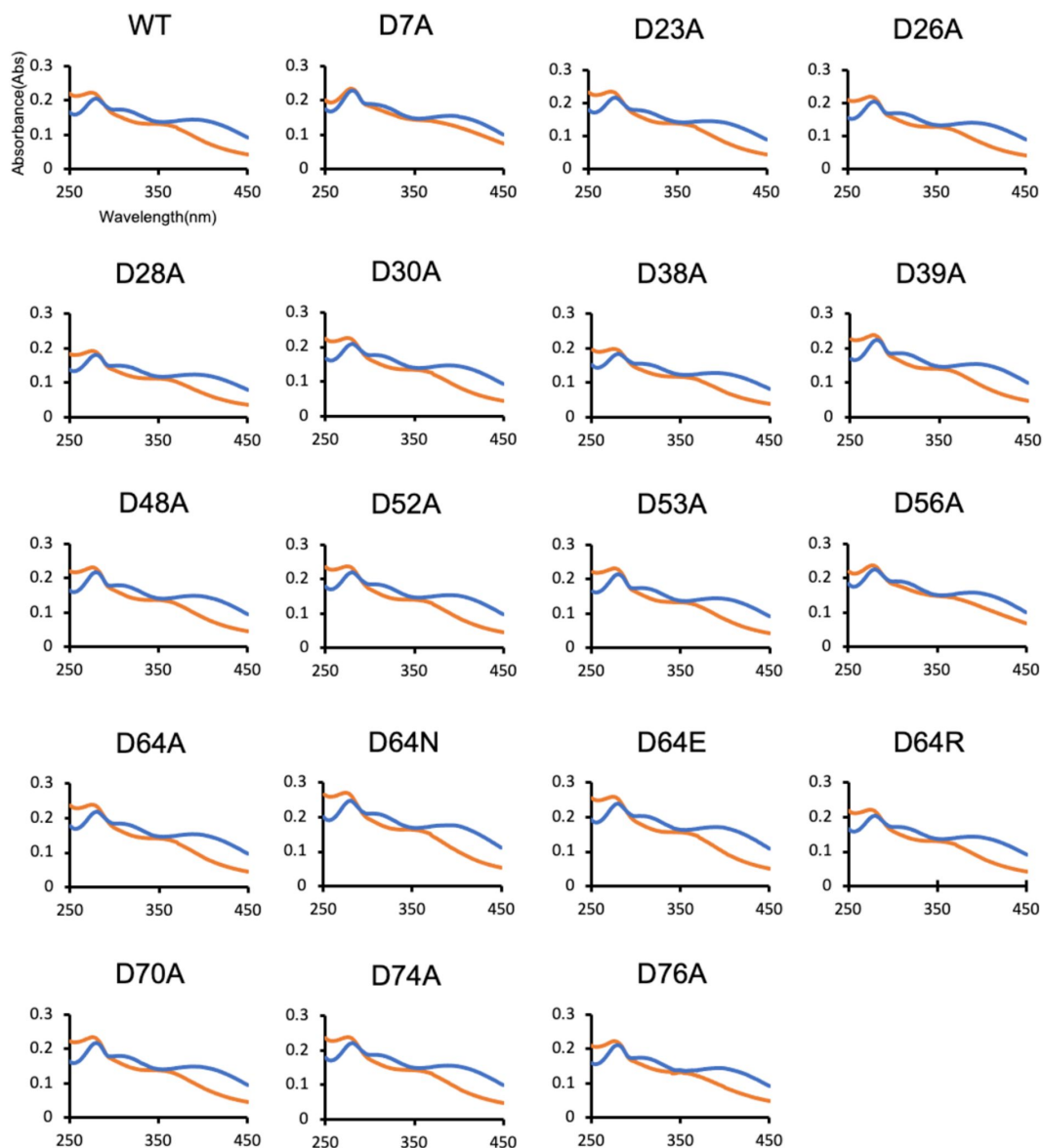


Fig. S4.

UV-Vis absorption spectroscopy of *BtFd* and its mutant proteins.

The spectra of reduced *BtFds* are indicated by the orange line and those of completely air-oxidized *BtFds* are indicated by the blue line. Wild-type *BtFd* and its mutated proteins showed very similar spectra.

Bacillaceae	DDMLDAFEGCP	SIKIADFP	DGDPLKFD
Alkalihalobacillus	EDMTDALEGCP	STRVADFP	EGDANKFE
Priestia	DDMHDAFEGCP	SIKVADFP	EGDALKYE
Bacillaceae	EDIMDAHDCGP	SIKVSDFP	DGDPNKKFE
Melghiribacillus thermohalophilus	EDMHDAFEGCP	SIKVSQSF	DGDPNKKFE
Bacillus wakoensis_JCM_9140	EDMHDAFEGCP	SIKIGDFP	DGDPLKFE
Pontibacillus	EDMHDAFEGCP	SIKVEDEF	DGDALKFE
Anaerobacillus alkaliphilus	DDMHDALEGCP	SIKIADFP	DGDALKFE
Bacillus sp._strain_OxB-1	DDITDAFDCGP	SIKMADEF	DGDPLKFE
Halobacillus	EDMHDAFEGCP	SIKVAEPF	NGDPLKFE
Pueribacillus theae	EDLEDAFEGCP	SIKISEFP	DGDPLKFE
Bacillaceae	DDLDDAFEGCP	SIKVSDFP	DGDPLKFE
Paralobacillus sp._G6-18	DDMLDAFEGCP	SIKLSKKCF	NGDPLKFE
Salinicoccus	DDLDDAFNGCP	SIKLAEPF	DGDPLKFE
Planococcaceae	EDLEDAFDCGP	SIKIADFP	DGDPLKFE
Bacillaceae	EDMHDAFEGCP	SIKIANDSF	DRDPPKFE
Halobacillus	EDMHDAFDCGP	SIKIAKSP	EGNAHKFE
Halobacillus litoralis	EDMHDALEGCP	SIKIAEPF	HGEPLKFE
Planococcaceae	EDMHDAFEGCP	SIKVADEF	DGDALKFE
Bacillus sp._PK3_68	EGLEDAFDCGP	SIKISDAS	DGDPNKKFE
Oceanobacillus manasiensis	EDMLDAFEGCP	SVKVSDFP	HGNPLKFE
Priestia endophytica	EEMLDAAFGCP	SIKVASAP	ENGMP....
Halalkalibacillus sediminis	EDLEDAFEGCP	SIKVSSEFP	EGDPNKKFE
Bacillus sp._OV194	DDAEDDALEGCP	SIKLGNEFP	ENGAN....
Sporosarcina sp._P13	DDLEDAFEGCP	SIKISDEF	QGNALKFE
Bacillaceae	DDLEDAFEGCP	SIKVGDEF	DPD....
Alkalihalobacillus patagoniensis	DDMLDAKDCGP	SIKCAKFP	DGNPLKFE
Paucisalibacillus globulus	DDVLDAAFGCP	SIKIAVNF	ENGNPTKFE
Salirhabdus	EDLEDAFDCGP	SIKISDKAF	DGDPNKKFE
Bacillus sp._IB182487	DDLDDAFEGCP	SIKIAEESF	EGNS....
Domibacillus antri	DDLEDAFEGCP	SIKIADSF	SED....
Sporolactobacillus pectinivorans	EDLEDAFEGCP	SIKIVADFP	HGSPKFE
Sporolactobacillus spathodeae	EDMHDAFDCGP	SVQISDFP
Bacillus sp._CRN9	DCIAFAFEGCP	SIKIAKAP	ENGNAKFE
Thermicanus aegyptius	EDMHDAFEGCP	SIKVSSEFP
Bacillus	DDLEDAFDCGP	SIKIAEPF	CA....
Bacillus sp._03113	DDLEDAFEGCP	SIKVADFP	ENGMP....
Virgibacillus halotolerans	EDVLDAAHDCGP	SIKISRCF	DGDPNKKFE
Bacillaceae	DDLEDAFEGCP	SIKISDFP	ENGMP....
Bacillus sp._UNC438CL73TsuS30	ADLVDAFDCGP	SIKVAEPF
Salicibacter cibarius	EDLVDAFEGCP	SIKVAEPF	HGDPKFE
Bacillus sp._OxB-1	DDLEDAFEGCP	SIKVAEPF
Terrabacteria	DDLEDAFEGCP	SIKVSDFP
Bacillales	EDLEDAFDCGP	SIKVSDFP
Desmospora activa DSM45169	EEVDDAFEGCP	SIKVE....
Domibacillus iocassae	DELEDAFEGCP	SIKVSDFP
Thermoactinomycetaceae	DDVDDAFEGCP	SIKVE....
Priestia endophytica	EDVDDAFEGCP	SIKIANEF
Cerasibacillus terrae	DDVLDAAHDCGP	SIKVSDFP	HGNPN1..
Paenisporosarcina	DDLEDAFEGCP	SIKVS....
Paenibacillus	DDMHDAFDCGP	SIKVAEPF	FNK....
Bacillaceae	EDVDDAFEGCP	SIKLSDFP	FN....
Cohnella	DDLDAAFDCGP	SIKVAEPF	FS....
Cohnella sp._OV330	DDLDAAFDCGP	SIKIAEPF	FN....
Bacillus sp._HF117_J1_D	DDVDDAFEGCP	SIKLSDFP	FK....
Paenibacillus	EDMHDAFDCGP	SIKIAEPF	FN....
Alteribacillus persepolensis	EDLEDAFEGCP	SIKVSDFP	FP....
Planococcaceae	DDLEDAFEGCP	SIKIANEF	YGNABKFD
Paenibacillaceae	DDVDDAFEGCP	SIKVE....
Tenuibacillus multivorans	DDLEDAFEGCP	SIKLSDFP	FN....
Saccharibacillus	EDMHDAFDCGP	SIKIAEPF	FNK....
Aneurinibacillus soli	DDVDDAFEGCP	SIKVE....
Alteribacillus iranensis	EDLEDAFEGCP	SIKVSSEFP	HGDPKFE
Paenibacillus hunanensis	EDMHDAFDCGP	SIKIAEPF	FN....
Terrabacteria group	DDVDDAFEGCP	SIKIAEPF	FN....
Sporolactobacillus sp._THM7-7	DDLEDAFEGCP	SIKVSDFP	ER....

Fig. S5.

Conserved amino acid residues of [4Fe-4S] ferredoxins from several species.

Cysteine residues for the ligand for the Fe-S cluster are completely conserved (orange-highlighted) and several residues around the cysteines are also highly conserved (blue-highlighted). The corresponding residues of Asp64 in BtFd are conserved in negatively charged residues (Asp or Glu; red-highlighted). This figure is prepared using ESript ver3.0 server (<https://esript.ibcp.fr/ESript/ESript/index.php>).

Fig. S6.

Sequence alignment of [4Fe-4S], [4Fe-4S]₂ and [3Fe-4S] ferredoxins from various organisms.

Cysteine residues for the ligand for the Fe-S cluster are completely conserved (yellow-highlighted) and several residues around the cysteines are also highly conserved (blue-highlighted). The corresponding residues of Asp64 in BtFd are conserved in negatively charged residues (Asp or Glu; pink font). This figure is prepared using the Consurf server (https://consurf.tau.ac.il/index_proteins.php) and ESript ver3.0 server (<https://esript.ibcp.fr/ESript/ESript/index.php>).

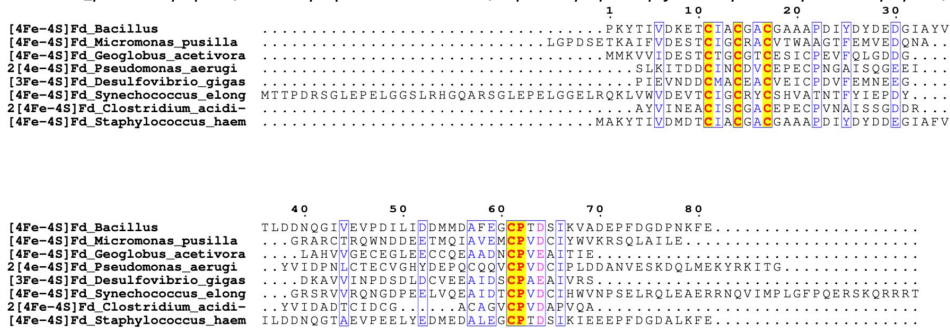


Fig. S7.

The pKa estimation of the Asp64 in BtFd

(A) A close-up view of an overlay of the of the CACO experiments (C β offset) of NMR. The assignments were indicated. For Asp64 signals, corresponding pH values are shown in blue as a representative of titrations. Chemical shift changes are indicated by black dotted line for each residue. Detail information were described in the supplemental method and text. (B) Titration curves obtained from the CACO experiments (C β offset). The points correspond to pH 7.0 and 7.5 are missing in a series of Asp64, and the point corresponds to pH 6.5 is missing in a series of Asp74. (C) The oxidation rates of BtFd wild-type and D64A under the different pH conditions.

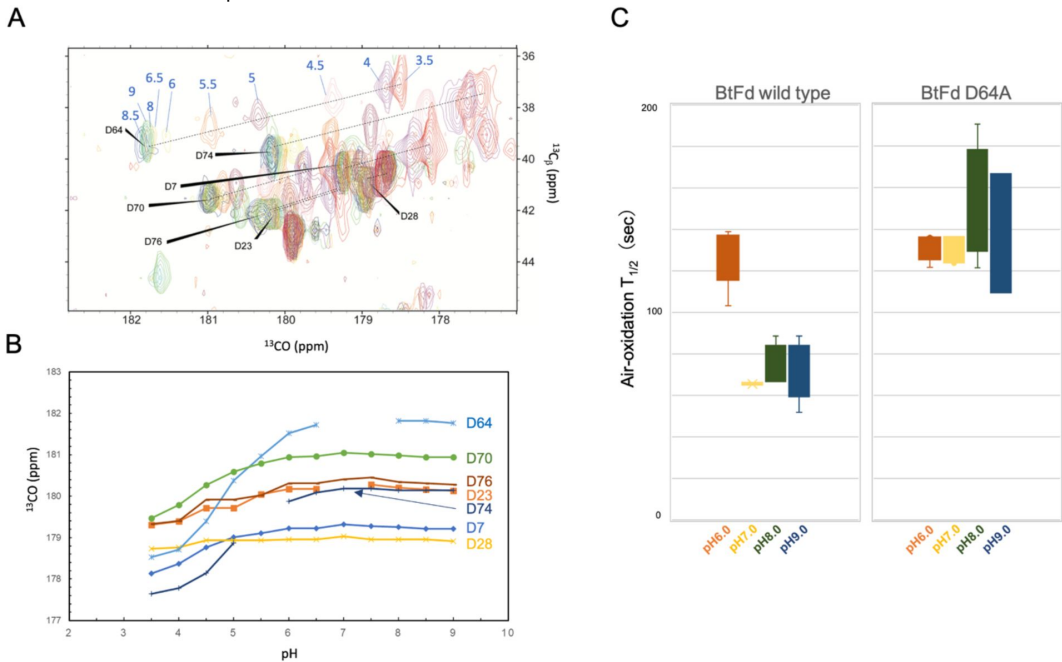


Fig. S8.

Stability of [4Fe-4S] cluster in *BtFd* under the different pH conditions.

The UV-Vis absorbance ratios of 304 nm/280 nm, 388 nm/280 nm and 304 nm/388 nm are shown in the table below each spectral panel.

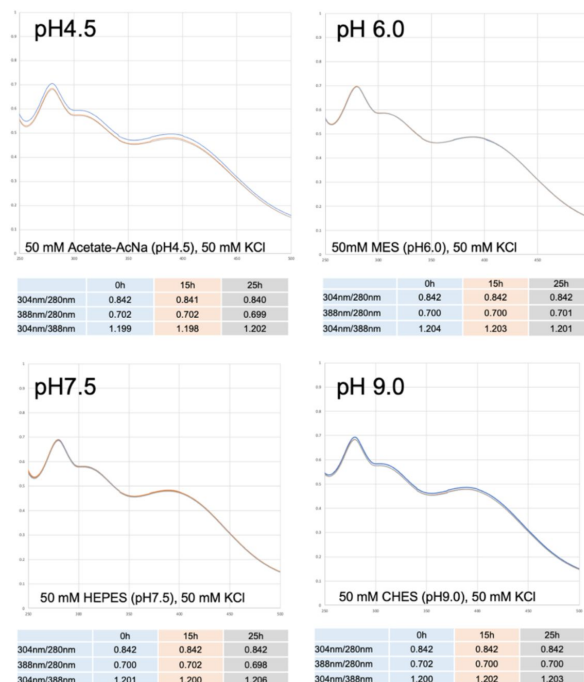
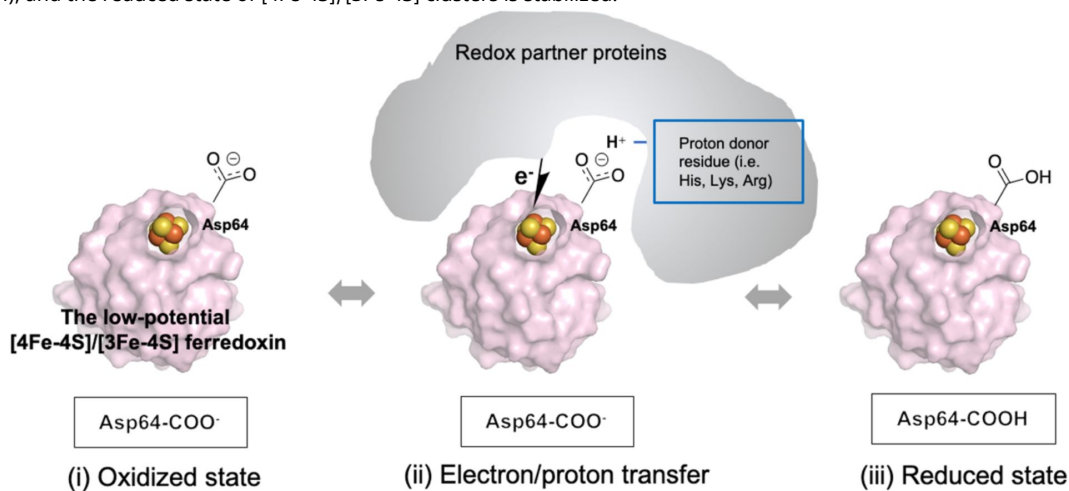


Fig. S9.

Proposed putative mechanism of the low-potential ferredoxin.

(i) The deprotonation state of the aspartate residue (Asp-COO⁻) neighboring the oxidized [4Fe-4S]/[3Fe-4S] cluster is the receivable state of an electron. (ii) When the electron-donor protein forms a complex with ferredoxin, the electrons move to the [4Fe-4S]/[3Fe-4S] cluster instantaneously. (iii) Next, the aspartate residue accepts the proton for neutralization (Asp-COOH), and the reduced state of [4Fe-4S]/[3Fe-4S] clusters is stabilized.



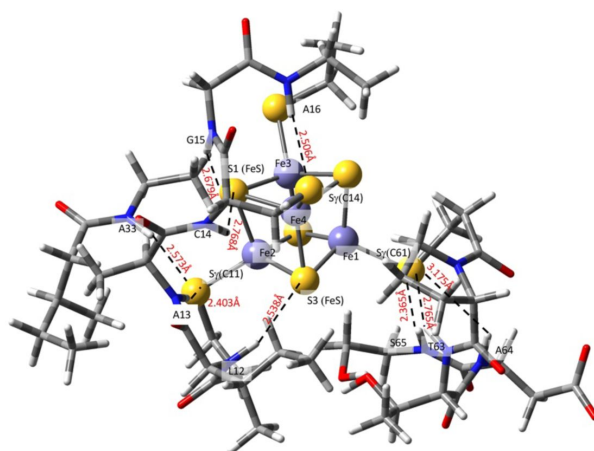
atom	x / Å	y / Å	z / Å	x / Å	y / Å	z / Å	x / Å
Fe	51.156	26.907	-3.179	C	54.743	28.460	-1.565
Fe	48.980	28.449	-3.585	H	56.554	27.390	0.793
Fe	50.443	27.558	-5.708	H	55.043	29.582	1.547
Fe	51.472	29.467	-3.999	H	56.424	29.637	0.416
S	49.681	29.696	-5.349	H	53.459	29.555	-0.186
S	52.523	27.621	-4.827	H	54.736	30.548	-0.942
S	50.558	28.775	-2.049	H	55.562	28.730	-2.232
S	49.293	26.313	-4.232	N	53.408	26.740	1.466
N	48.058	30.492	-0.277	C	52.479	26.302	2.502
C	48.219	31.919	-0.009	C	52.033	24.858	2.334
C	48.373	32.739	-1.294	O	51.037	24.440	2.919
O	48.790	33.898	-1.240	C	51.274	27.224	2.544
C	49.362	32.179	0.994	O	50.717	27.319	1.226
C	50.663	31.594	0.458	C	51.683	28.622	3.012
C	49.044	31.580	2.341	H	52.994	26.365	3.461
C	51.905	32.039	1.231	H	50.532	26.832	3.239
H	47.297	32.268	0.456	H	50.801	29.255	3.109
H	49.470	33.257	1.113	H	52.182	28.559	3.980
H	50.608	30.506	0.515	H	52.365	29.072	2.291
H	50.788	31.907	-0.579	H	52.996	26.764	0.533
H	49.851	31.818	3.035	H	49.739	27.288	1.273
H	48.106	32.000	2.704	N	52.739	24.097	1.524
H	48.952	30.499	2.237	C	52.447	22.665	1.388
H	51.935	31.514	2.186	C	50.999	22.421	0.957
H	52.792	31.797	0.647	O	50.377	21.434	1.348
H	51.851	33.114	1.399	C	52.807	21.865	2.656
H	48.919	30.035	-0.577	C	54.316	21.837	2.927
N	48.006	32.177	-2.459	O	55.107	21.756	1.965
C	47.922	32.940	-3.709	H	53.083	22.274	0.594
C	49.249	33.579	-4.101	H	52.318	22.322	3.516
O	49.289	34.735	-4.534	H	52.466	20.836	2.537
C	46.811	33.991	-3.658	H	53.515	24.428	0.950
H	47.015	34.684	-2.842	N	50.463	23.310	0.125
H	46.787	34.530	-4.605	C	48.604	24.612	-0.759
H	45.856	33.492	-3.491	O	48.641	25.501	0.378
H	47.761	31.192	-2.562	H	49.257	24.999	-1.542
N	50.339	32.821	-3.970	H	47.581	24.541	-1.129
C	51.682	33.345	-4.188	H	50.971	24.109	-0.253
C	52.133	33.338	-5.642	H	49.569	25.652	0.655
O	53.113	34.018	-5.958	H	53.842	28.258	-2.144
C	52.691	32.574	-3.340	C	54.867	25.648	-2.573

Table S1.

Cartesian coordinate of CM_H used for the DFT calculations

S	53.161	30.980	-3.986	H	55.881	25.386	-2.790
H	51.680	34.387	-3.867	H	54.491	26.286	-3.345
H	53.599	33.172	-3.255	C	49.084	23.239	-0.339
H	52.258	32.412	-2.353	H	48.350	22.946	0.382
H	50.323	31.834	-3.713	H	49.166	22.483	-1.092
N	51.471	32.597	-6.531	O	54.717	21.901	4.118
C	51.828	32.597	-7.941	H	55.079	21.052	4.381
C	52.971	31.678	-8.370	C	44.136	29.698	-6.554
O	53.291	31.646	-9.569	O	43.373	29.594	-7.527
H	50.948	32.303	-8.513	C	42.720	30.361	-4.590
H	52.110	33.612	-8.220	C	42.430	31.428	-3.521
H	50.685	31.990	-6.300	C	42.981	29.008	-3.942
N	53.583	30.912	-7.458	C	43.569	31.718	-2.601
C	55.472	29.647	-6.552	H	41.838	30.289	-5.226
H	55.963	30.501	-6.085	H	42.169	32.359	-4.023
H	54.745	29.214	-5.865	H	41.594	31.087	-2.910
H	56.214	28.897	-6.829	H	43.199	28.278	-4.721
H	53.297	30.825	-6.483	H	43.831	29.097	-3.266
C	46.889	29.856	-0.139	H	42.094	28.705	-3.386
H	47.678	32.225	-4.495	H	43.174	31.997	-1.624
S	46.811	29.076	-3.190	H	44.189	30.826	-2.510
C	46.231	28.098	-1.820	H	44.157	32.539	-3.012
H	45.445	28.621	-1.316	N	45.177	28.897	-6.365
H	45.862	27.161	-2.182	C	46.957	27.364	-7.072
O	45.859	30.407	0.236	H	47.143	26.500	-7.710
C	46.900	28.370	-0.456	H	47.689	28.145	-7.280
H	46.342	27.619	0.062	H	47.015	27.070	-6.024
H	47.940	28.260	-0.231	H	45.775	28.909	-5.539
C	54.749	30.117	-7.808	C	45.558	27.903	-7.361
H	55.572	30.565	-8.324	H	45.577	28.326	-8.344
H	54.248	29.433	-8.461	H	44.800	27.150	-7.311
C	55.189	26.023	-1.124	C	43.907	30.756	-5.480
O	55.475	25.135	-0.325	H	44.808	30.834	-4.908
C	53.647	24.744	-2.630	H	43.682	31.704	-5.922
S	52.213	25.438	-1.764	C	51.979	26.168	-8.183
H	53.369	24.590	-3.673	S	50.437	27.038	-7.918
H	53.892	23.789	-2.165	H	51.743	25.253	-8.726
N	55.102	27.304	-0.742	H	52.385	25.925	-7.201
C	55.518	27.685	0.626	C	53.058	26.931	-8.974
C	54.676	27.075	1.726	H	52.720	27.928	-9.167
O	55.181	26.899	2.841	H	53.962	26.965	-8.403
C	55.433	29.219	0.596	H	53.241	26.430	-9.902
C	54.492	29.567	-0.536				

Table S1. (continued)



(A) Oxidized (Ox) state (u and d represent up and down spins)

Examined states	Fe1	Fe2	Fe3	Fe4	Energy / Hartree
charge	2	2	3	3	
o1	u	d	u	d	-8400.022791
o2	u	d	d	u	-8400.025020
charge	2	3	2	3	
o3	u	u	d	d	-8399.983854
o4	u	d	d	u	-8400.025019
charge	2	3	3	2	
o5	u	u	d	d	-8400.022702
o6	u	d	u	d	-8400.022789
charge	3	2	3	2	
o7	u	u	d	d	-8400.022689
o8	d	u	u	d	-8400.025019
charge	3	2	2	3	
o9	u	u	d	d	-8400.022693
o10	d	u	d	u	-8400.022801
charge	3	3	2	2	
o11	u	d	u	d	-8400.022802
o12	d	u	u	d	-8400.025022

Table S2.

Examined charge/spin states with CM_{NA} model for (A) oxidized and (B) reduced states. Definition of Fe1-Fe4 is illustrated using CM below. o12 and r5 (indicated by yellow highlighted) were most stable states for Ox and Red states, respectively.

(B) Reduced (<i>Red</i>) state (u and d represent up and down spins)					
Examined states	Fe1	Fe2	Fe3	Fe4	Energy / Hartree
charge	3	2	2	2	
r1	u	u	d	d	-8399.871923
r2	u	d	u	d	-8399.870871
r3	u	d	d	u	-8399.871694
charge	2	3	2	2	
r4	u	u	d	d	-8399.871876
r5	d	u	u	d	-8399.872594
r6	d	u	d	u	-8399.869132
charge	2	2	3	2	
r7	u	d	u	d	-8399.870871
r8	d	u	u	d	-8399.872589
r9	d	d	u	u	-8399.867054
charge	2	2	2	3	
r10	u	d	d	u	-8399.871693
r11	d	u	d	u	-8399.869131
r12	d	d	u	u	-8399.656590

Table S2. (continued)

Part 1. CM model

Before optimization				After optimization			
Fe	51.1560	26.9070	-3.1790	Fe	51.0899	26.8241	-3.0748
Fe	48.9800	28.4490	-3.5850	Fe	48.9077	28.4118	-3.6890
Fe	50.4430	27.5580	-5.7080	Fe	50.4026	27.5837	-5.8198
Fe	51.4720	29.4670	-3.9990	Fe	51.5173	29.5281	-4.0769
S	49.6810	29.6960	-5.3490	S	49.6463	29.7914	-5.5251
S	52.5230	27.6210	-4.8270	S	52.5245	27.5200	-4.9853
S	50.5580	28.7750	-2.0490	S	50.4549	28.9082	-2.0530
S	49.2930	26.3130	-4.2320	S	49.2273	26.1675	-4.3358
N	48.0580	30.4920	-0.2770	N	48.0580	30.4920	-0.2770
C	48.2190	31.9190	-0.0090	C	48.2190	31.9190	-0.0090
C	48.3730	32.7390	-1.2940	C	48.3730	32.7390	-1.2940
O	48.7900	33.8980	-1.2400	O	48.7900	33.8980	-1.2400
C	49.3620	32.1790	0.9940	C	49.3620	32.1790	0.9940
C	50.6630	31.5940	0.4580	C	50.6630	31.5940	0.4580
C	49.0440	31.5800	2.3410	C	49.0440	31.5800	2.3410
C	51.9050	32.0390	1.2310	C	51.9050	32.0390	1.2310
H	47.2970	32.2680	0.4560	H	47.2970	32.2680	0.4560
H	49.4700	33.2570	1.1130	H	49.4700	33.2570	1.1130
H	50.6080	30.5060	0.5150	H	50.6080	30.5060	0.5150
H	50.7880	31.9070	-0.5790	H	50.7880	31.9070	-0.5790
H	49.8510	31.8180	3.0350	H	49.8510	31.8180	3.0350
H	48.1060	32.0000	2.7040	H	48.1060	32.0000	2.7040
H	48.9520	30.4990	2.2370	H	48.9520	30.4990	2.2370
H	51.9350	31.5140	2.1860	H	51.9350	31.5140	2.1860
H	52.7920	31.7970	0.6470	H	52.7920	31.7970	0.6470
H	51.8510	33.1140	1.3990	H	51.8510	33.1140	1.3990
H	48.9190	30.0350	-0.5770	H	48.9190	30.0350	-0.5770
N	48.0060	32.1770	-2.4590	N	48.0060	32.1770	-2.4590
C	47.9220	32.9400	-3.7090	C	47.9220	32.9400	-3.7090

Table S3.

Cartesian coordinate (in Å) of before and after the geometry optimization. (The Cartesian coordinate before the geometry optimization is the neutron structure)

C	49.2490	33.5790	-4.1010	C	49.2490	33.5790	-4.1010
O	49.2890	34.7350	-4.5340	O	49.2890	34.7350	-4.5340
C	46.8110	33.9910	-3.6580	C	46.8110	33.9910	-3.6580
H	47.0150	34.6840	-2.8420	H	47.0150	34.6840	-2.8420
H	46.7870	34.5300	-4.6050	H	46.7870	34.5300	-4.6050
H	45.8560	33.4920	-3.4910	H	45.8560	33.4920	-3.4910
H	47.7610	31.1920	-2.5620	H	47.7610	31.1920	-2.5620
N	50.3390	32.8210	-3.9700	N	50.3390	32.8210	-3.9700
C	51.6820	33.3450	-4.1880	C	51.6821	33.3451	-4.1880
C	52.1330	33.3380	-5.6420	C	52.1330	33.3380	-5.6420
O	53.1130	34.0180	-5.9580	O	53.1130	34.0180	-5.9580
C	52.6910	32.5740	-3.3400	C	52.6908	32.5738	-3.3400
S	53.1610	30.9800	-3.9860	S	53.2923	30.9518	-3.9777
H	51.6800	34.3870	-3.8670	H	51.6800	34.3870	-3.8670
H	53.5990	33.1720	-3.2550	H	53.5990	33.1720	-3.2550
H	52.2580	32.4120	-2.3530	H	52.2581	32.4121	-2.3530
H	50.3230	31.8340	-3.7130	H	50.3230	31.8340	-3.7130
N	51.4710	32.5970	-6.5310	N	51.4710	32.5970	-6.5310
C	51.8280	32.5970	-7.9410	C	51.8280	32.5970	-7.9410
C	52.9710	31.6780	-8.3700	C	52.9710	31.6780	-8.3700
O	53.2910	31.6460	-9.5690	O	53.2910	31.6460	-9.5690
H	50.9480	32.3030	-8.5130	H	50.9480	32.3030	-8.5130
H	52.1100	33.6120	-8.2200	H	52.1100	33.6120	-8.2200
H	50.6850	31.9900	-6.3000	H	50.6850	31.9900	-6.3000
N	53.5830	30.9120	-7.4580	N	53.5830	30.9120	-7.4580
C	55.4720	29.6470	-6.5520	C	55.4720	29.6470	-6.5520
H	55.9630	30.5010	-6.0850	H	55.9630	30.5010	-6.0850
H	54.7450	29.2140	-5.8650	H	54.7450	29.2140	-5.8650
H	56.2140	28.8970	-6.8290	H	56.2140	28.8970	-6.8290
H	53.2970	30.8250	-6.4830	H	53.2970	30.8250	-6.4830
C	46.8895	29.8555	-0.1395	C	46.8895	29.8555	-0.1395
H	47.6780	32.2250	-4.4950	H	47.6780	32.2250	-4.4950

Table S3. (continued)

S	46.8110	29.0760	-3.1900	S	46.7360	29.1131	-3.2770
C	46.2315	28.0983	-1.8201	C	46.2318	28.0982	-1.8202
H	45.4454	28.6209	-1.3162	H	45.4454	28.6209	-1.3162
H	45.8624	27.1613	-2.1815	H	45.8623	27.1613	-2.1815
O	45.8590	30.4070	0.2360	O	45.8590	30.4070	0.2360
C	46.9000	28.3700	-0.4560	C	46.8999	28.3701	-0.4560
H	46.3416	27.6187	0.0623	H	46.3415	27.6187	0.0623
H	47.9403	28.2600	-0.2310	H	47.9403	28.2599	-0.2310
C	54.7490	30.1170	-7.8080	C	54.7490	30.1170	-7.8080
H	55.5724	30.5645	-8.3243	H	55.5724	30.5645	-8.3243
H	54.2480	29.4329	-8.4607	H	54.2480	29.4329	-8.4607
C	55.1890	26.0230	-1.1240	C	55.1890	26.0230	-1.1240
O	55.4750	25.1350	-0.3250	O	55.4750	25.1350	-0.3250
C	53.6470	24.7440	-2.6300	C	53.6470	24.7441	-2.6301
S	52.2130	25.4380	-1.7640	S	52.2470	25.4672	-1.6975
H	53.3690	24.5900	-3.6730	H	53.3690	24.5900	-3.6730
H	53.8920	23.7890	-2.1650	H	53.8920	23.7890	-2.1650
N	55.1020	27.3040	-0.7420	N	55.1020	27.3040	-0.7420
C	55.5180	27.6850	0.6260	C	55.5180	27.6850	0.6260
C	54.6760	27.0750	1.7260	C	54.6760	27.0750	1.7260
O	55.1810	26.8990	2.8410	O	55.1810	26.8990	2.8410
C	55.4330	29.2190	0.5960	C	55.4330	29.2190	0.5960
C	54.4920	29.5670	-0.5360	C	54.4920	29.5670	-0.5360
C	54.7430	28.4600	-1.5650	C	54.7430	28.4600	-1.5650
H	56.5540	27.3900	0.7930	H	56.5540	27.3900	0.7930
H	55.0430	29.5820	1.5470	H	55.0430	29.5820	1.5470
H	56.4240	29.6370	0.4160	H	56.4240	29.6370	0.4160
H	53.4590	29.5550	-0.1860	H	53.4590	29.5550	-0.1860
H	54.7360	30.5480	-0.9420	H	54.7360	30.5480	-0.9420
H	55.5620	28.7300	-2.2320	H	55.5620	28.7300	-2.2320
N	53.4080	26.7400	1.4660	N	53.4080	26.7400	1.4660
C	52.4790	26.3020	2.5020	C	52.4790	26.3020	2.5020

Table S3. (continued)

C	52.0330	24.8580	2.3340	C	52.0330	24.8580	2.3340
O	51.0370	24.4400	2.9190	O	51.0370	24.4400	2.9190
C	51.2740	27.2240	2.5440	C	51.2740	27.2240	2.5440
O	50.7170	27.3190	1.2260	O	50.7170	27.3190	1.2260
C	51.6830	28.6220	3.0120	C	51.6830	28.6220	3.0120
H	52.9940	26.3650	3.4610	H	52.9940	26.3650	3.4610
H	50.5320	26.8320	3.2390	H	50.5320	26.8320	3.2390
H	50.8010	29.2550	3.1090	H	50.8010	29.2550	3.1090
H	52.1820	28.5590	3.9800	H	52.1820	28.5590	3.9800
H	52.3650	29.0720	2.2910	H	52.3650	29.0720	2.2910
H	52.9960	26.7640	0.5330	H	52.9960	26.7640	0.5330
H	49.7390	27.2880	1.2730	H	49.7390	27.2880	1.2730
N	52.7390	24.0970	1.5240	N	52.7390	24.0970	1.5240
C	52.4470	22.6650	1.3880	C	52.4470	22.6650	1.3880
C	50.9990	22.4210	0.9570	C	50.9990	22.4210	0.9570
O	50.3770	21.4340	1.3480	O	50.3770	21.4340	1.3480
C	52.8070	21.8650	2.6560	C	52.8070	21.8650	2.6560
C	54.3160	21.8370	2.9270	C	54.3160	21.8370	2.9270
O	55.1070	21.7560	1.9650	O	55.1070	21.7560	1.9650
O	54.7150	21.9010	4.1110	O	54.7150	21.9010	4.1110
H	53.0830	22.2740	0.5940	H	53.0830	22.2740	0.5940
H	52.3180	22.3220	3.5160	H	52.3180	22.3220	3.5160
H	52.4660	20.8360	2.5370	H	52.4660	20.8360	2.5370
H	53.5150	24.4280	0.9500	H	53.5150	24.4280	0.9500
N	50.4630	23.3100	0.1250	N	50.4630	23.3100	0.1250
C	48.6040	24.6120	-0.7590	C	48.6040	24.6120	-0.7590
O	48.6410	25.5010	0.3780	O	48.6410	25.5010	0.3780
H	49.2570	24.9990	-1.5420	H	49.2570	24.9990	-1.5420
H	47.5810	24.5410	-1.1290	H	47.5810	24.5410	-1.1290
H	50.9710	24.1090	-0.2530	H	50.9710	24.1090	-0.2530
H	49.5690	25.6520	0.6550	H	49.5690	25.6520	0.6550
H	53.8420	28.2580	-2.1440	H	53.8420	28.2580	-2.1440

Table S3. (continued)

C	54.8670	25.6480	-2.5730	C	54.8670	25.6480	-2.5730
H	55.8815	25.3859	-2.7899	H	55.8815	25.3859	-2.7899
H	54.4906	26.2860	-3.3451	H	54.4906	26.2860	-3.3451
C	49.0840	23.2390	-0.3390	C	49.0840	23.2390	-0.3390
H	48.3495	22.9463	0.3820	H	48.3495	22.9463	0.3820
H	49.1657	22.4831	-1.0919	H	49.1657	22.4831	-1.0919
C	44.1360	29.6980	-6.5540	C	44.1360	29.6980	-6.5540
O	43.3730	29.5940	-7.5270	O	43.3730	29.5940	-7.5270
C	42.7200	30.3610	-4.5900	C	42.7200	30.3610	-4.5900
C	42.4300	31.4280	-3.5210	C	42.4300	31.4280	-3.5210
C	42.9810	29.0080	-3.9420	C	42.9810	29.0080	-3.9420
C	43.5690	31.7180	-2.6010	C	43.5690	31.7180	-2.6010
H	41.8380	30.2890	-5.2260	H	41.8380	30.2890	-5.2260
H	42.1690	32.3590	-4.0230	H	42.1690	32.3590	-4.0230
H	41.5940	31.0870	-2.9100	H	41.5940	31.0870	-2.9100
H	43.1990	28.2780	-4.7210	H	43.1990	28.2780	-4.7210
H	43.8310	29.0970	-3.2660	H	43.8310	29.0970	-3.2660
H	42.0940	28.7050	-3.3860	H	42.0940	28.7050	-3.3860
H	43.1740	31.9970	-1.6240	H	43.1740	31.9970	-1.6240
H	44.1890	30.8260	-2.5100	H	44.1890	30.8260	-2.5100
H	44.1570	32.5390	-3.0120	H	44.1570	32.5390	-3.0120
N	45.1770	28.8970	-6.3650	N	45.1770	28.8970	-6.3650
C	46.9570	27.3640	-7.0720	C	46.9570	27.3640	-7.0720
H	47.1430	26.5000	-7.7100	H	47.1430	26.5000	-7.7100
H	47.6890	28.1450	-7.2800	H	47.6890	28.1450	-7.2800
H	47.0150	27.0700	-6.0240	H	47.0150	27.0700	-6.0240
H	45.7750	28.9090	-5.5390	H	45.7750	28.9090	-5.5390
C	45.5580	27.9030	-7.3610	C	45.5580	27.9030	-7.3610
H	45.5770	28.3258	-8.3437	H	45.5770	28.3258	-8.3437
H	44.7997	27.1498	-7.3114	H	44.7997	27.1498	-7.3114
C	43.9070	30.7560	-5.4800	C	43.9070	30.7560	-5.4800
H	44.8080	30.8336	-4.9080	H	44.8080	30.8336	-4.9080

Table S3. (continued)

H	43.6824	31.7042	-5.9221	H	43.6824	31.7042	-5.9221
C	51.9790	26.1680	-8.1830	C	51.9790	26.1682	-8.1826
S	50.4370	27.0380	-7.9180	S	50.3589	27.0411	-8.0554
H	51.7430	25.2530	-8.7260	H	51.7430	25.2530	-8.7261
H	52.3850	25.9250	-7.2010	H	52.3850	25.9249	-7.2010
C	53.0578	26.9308	-8.9741	C	53.0578	26.9307	-8.9743
H	52.7204	27.9276	-9.1674	H	52.7204	27.9276	-9.1673
H	53.9619	26.9647	-8.4028	H	53.9619	26.9647	-8.4029
H	53.2407	26.4300	-9.9018	H	53.2407	26.4300	-9.9019

Part 2. CM_H model

Before optimization				After optimization			
Fe	51.1560	26.9070	-3.1790	Fe	51.0943	26.8246	-3.0613
Fe	48.9800	28.4489	-3.5851	Fe	48.9111	28.3918	-3.6611
Fe	50.4430	27.5580	-5.7080	Fe	50.4148	27.5566	-5.7999
Fe	51.4720	29.4670	-3.9990	Fe	51.5223	29.5247	-4.0565
S	49.6810	29.6960	-5.3490	S	49.6625	29.7604	-5.4967
S	52.5230	27.6210	-4.8270	S	52.5387	27.4961	-4.9493
S	50.5580	28.7750	-2.0490	S	50.4679	28.8805	-2.0194
S	49.2930	26.3130	-4.2320	S	49.2421	26.1403	-4.3041
N	48.0580	30.4920	-0.2770	N	48.0580	30.4920	-0.2770
C	48.2190	31.9190	-0.0090	C	48.2190	31.9190	-0.0090
C	48.3730	32.7390	-1.2940	C	48.3730	32.7390	-1.2940
O	48.7900	33.8980	-1.2400	O	48.7900	33.8980	-1.2400
C	49.3620	32.1790	0.9940	C	49.3620	32.1790	0.9940
C	50.6630	31.5940	0.4580	C	50.6630	31.5940	0.4580
C	49.0440	31.5800	2.3410	C	49.0440	31.5800	2.3410
C	51.9050	32.0390	1.2310	C	51.9050	32.0390	1.2310
H	47.2970	32.2680	0.4560	H	47.2970	32.2680	0.4560
H	49.4700	33.2570	1.1130	H	49.4700	33.2570	1.1130

Table S3. (continued)

H	50.6080	30.5060	0.5150	H	50.6080	30.5060	0.5150
H	50.7880	31.9070	-0.5790	H	50.7880	31.9070	-0.5790
H	49.8510	31.8180	3.0350	H	49.8510	31.8180	3.0350
H	48.1060	32.0000	2.7040	H	48.1060	32.0000	2.7040
H	48.9520	30.4990	2.2370	H	48.9520	30.4990	2.2370
H	51.9350	31.5140	2.1860	H	51.9350	31.5140	2.1860
H	52.7920	31.7970	0.6470	H	52.7920	31.7970	0.6470
H	51.8510	33.1140	1.3990	H	51.8510	33.1140	1.3990
H	48.9190	30.0350	-0.5770	H	48.9190	30.0350	-0.5770
N	48.0060	32.1770	-2.4590	N	48.0060	32.1770	-2.4590
C	47.9220	32.9400	-3.7090	C	47.9220	32.9400	-3.7090
C	49.2490	33.5790	-4.1010	C	49.2490	33.5790	-4.1010
O	49.2890	34.7350	-4.5340	O	49.2890	34.7350	-4.5340
C	46.8110	33.9910	-3.6580	C	46.8110	33.9910	-3.6580
H	47.0150	34.6840	-2.8420	H	47.0150	34.6840	-2.8420
H	46.7870	34.5300	-4.6050	H	46.7870	34.5300	-4.6050
H	45.8560	33.4920	-3.4910	H	45.8560	33.4920	-3.4910
H	47.7610	31.1920	-2.5620	H	47.7610	31.1920	-2.5620
N	50.3390	32.8210	-3.9700	N	50.3390	32.8210	-3.9700
C	51.6820	33.3450	-4.1880	C	51.6820	33.3451	-4.1880
C	52.1330	33.3380	-5.6420	C	52.1330	33.3380	-5.6420
O	53.1130	34.0180	-5.9580	O	53.1130	34.0180	-5.9580
C	52.6910	32.5740	-3.3400	C	52.6908	32.5738	-3.3400
S	53.1610	30.9800	-3.9860	S	53.2990	30.9481	-3.9670
H	51.6800	34.3870	-3.8670	H	51.6800	34.3870	-3.8670
H	53.5990	33.1720	-3.2550	H	53.5990	33.1720	-3.2550
H	52.2580	32.4120	-2.3530	H	52.2581	32.4121	-2.3530
H	50.3230	31.8340	-3.7130	H	50.3230	31.8340	-3.7130
N	51.4710	32.5970	-6.5310	N	51.4710	32.5970	-6.5310
C	51.8280	32.5970	-7.9410	C	51.8280	32.5970	-7.9410
C	52.9710	31.6780	-8.3700	C	52.9710	31.6780	-8.3700
O	53.2910	31.6460	-9.5690	O	53.2910	31.6460	-9.5690

Table S3. (continued)

H	50.9480	32.3030	-8.5130	H	50.9480	32.3030	-8.5130
H	52.1100	33.6120	-8.2200	H	52.1100	33.6120	-8.2200
H	50.6850	31.9900	-6.3000	H	50.6850	31.9900	-6.3000
N	53.5830	30.9120	-7.4580	N	53.5830	30.9120	-7.4580
C	55.4720	29.6470	-6.5520	C	55.4720	29.6470	-6.5520
H	55.9630	30.5010	-6.0850	H	55.9630	30.5010	-6.0850
H	54.7450	29.2140	-5.8650	H	54.7450	29.2140	-5.8650
H	56.2140	28.8970	-6.8290	H	56.2140	28.8970	-6.8290
H	53.2970	30.8250	-6.4830	H	53.2970	30.8250	-6.4830
C	46.8895	29.8555	-0.1395	C	46.8895	29.8555	-0.1395
H	47.6780	32.2250	-4.4950	H	47.6780	32.2250	-4.4950
S	46.8110	29.0760	-3.1900	S	46.7475	29.1063	-3.2748
C	46.2315	28.0983	-1.8201	C	46.2318	28.0982	-1.8202
H	45.4454	28.6209	-1.3162	H	45.4454	28.6209	-1.3163
H	45.8624	27.1613	-2.1815	H	45.8623	27.1613	-2.1815
O	45.8590	30.4070	0.2360	O	45.8590	30.4070	0.2360
C	46.9000	28.3700	-0.4560	C	46.8999	28.3701	-0.4560
H	46.3416	27.6187	0.0623	H	46.3415	27.6187	0.0623
H	47.9403	28.2600	-0.2310	H	47.9403	28.2599	-0.2310
C	54.7490	30.1170	-7.8080	C	54.7490	30.1170	-7.8080
H	55.5724	30.5645	-8.3243	H	55.5724	30.5645	-8.3244
H	54.2481	29.4329	-8.4607	H	54.2481	29.4329	-8.4607
C	55.1890	26.0230	-1.1240	C	55.1890	26.0230	-1.1240
O	55.4750	25.1350	-0.3250	O	55.4750	25.1350	-0.3250
C	53.6470	24.7440	-2.6300	C	53.6469	24.7441	-2.6301
S	52.2130	25.4380	-1.7640	S	52.2521	25.4563	-1.6763
H	53.3690	24.5900	-3.6730	H	53.3690	24.5900	-3.6730
H	53.8920	23.7890	-2.1650	H	53.8920	23.7890	-2.1650
N	55.1020	27.3040	-0.7420	N	55.1020	27.3040	-0.7420
C	55.5180	27.6850	0.6260	C	55.5180	27.6850	0.6260
C	54.6760	27.0750	1.7260	C	54.6760	27.0750	1.7260
O	55.1810	26.8990	2.8410	O	55.1810	26.8990	2.8410

Table S3. (continued)

C	55.4330	29.2190	0.5960	C	55.4330	29.2190	0.5960
C	54.4920	29.5670	-0.5360	C	54.4920	29.5670	-0.5360
C	54.7430	28.4600	-1.5650	C	54.7430	28.4600	-1.5650
H	56.5540	27.3900	0.7930	H	56.5540	27.3900	0.7930
H	55.0430	29.5820	1.5470	H	55.0430	29.5820	1.5470
H	56.4240	29.6370	0.4160	H	56.4240	29.6370	0.4160
H	53.4590	29.5550	-0.1860	H	53.4590	29.5550	-0.1860
H	54.7360	30.5480	-0.9420	H	54.7360	30.5480	-0.9420
H	55.5620	28.7300	-2.2320	H	55.5620	28.7300	-2.2320
N	53.4080	26.7400	1.4660	N	53.4080	26.7400	1.4660
C	52.4790	26.3020	2.5020	C	52.4790	26.3020	2.5020
C	52.0330	24.8580	2.3340	C	52.0330	24.8580	2.3340
O	51.0370	24.4400	2.9190	O	51.0370	24.4400	2.9190
C	51.2740	27.2240	2.5440	C	51.2740	27.2240	2.5440
O	50.7170	27.3190	1.2260	O	50.7170	27.3190	1.2260
C	51.6830	28.6220	3.0120	C	51.6830	28.6220	3.0120
H	52.9940	26.3650	3.4610	H	52.9940	26.3650	3.4610
H	50.5320	26.8320	3.2390	H	50.5320	26.8320	3.2390
H	50.8010	29.2550	3.1090	H	50.8010	29.2550	3.1090
H	52.1820	28.5590	3.9800	H	52.1820	28.5590	3.9800
H	52.3650	29.0720	2.2910	H	52.3650	29.0720	2.2910
H	52.9960	26.7640	0.5330	H	52.9960	26.7640	0.5330
H	49.7390	27.2880	1.2730	H	49.7390	27.2880	1.2730
N	52.7390	24.0970	1.5240	N	52.7390	24.0970	1.5240
C	52.4470	22.6650	1.3880	C	52.4470	22.6650	1.3880
C	50.9990	22.4210	0.9570	C	50.9990	22.4210	0.9570
O	50.3770	21.4340	1.3480	O	50.3770	21.4340	1.3480
C	52.8070	21.8650	2.6560	C	52.8070	21.8650	2.6560
C	54.3160	21.8370	2.9270	C	54.3160	21.8370	2.9270
O	55.1070	21.7560	1.9650	O	55.1070	21.7560	1.9650
H	53.0830	22.2740	0.5940	H	53.0830	22.2740	0.5940
H	52.3180	22.3220	3.5160	H	52.3180	22.3220	3.5160

Table S3. (continued)

H	52.4660	20.8360	2.5370	H	52.4660	20.8360	2.5370
H	53.5150	24.4280	0.9500	H	53.5150	24.4280	0.9500
N	50.4630	23.3100	0.1250	N	50.4630	23.3100	0.1250
C	48.6040	24.6120	-0.7590	C	48.6040	24.6120	-0.7590
O	48.6410	25.5010	0.3780	O	48.6410	25.5010	0.3780
H	49.2570	24.9990	-1.5420	H	49.2570	24.9990	-1.5420
H	47.5810	24.5410	-1.1290	H	47.5810	24.5410	-1.1290
H	50.9710	24.1090	-0.2530	H	50.9710	24.1090	-0.2530
H	49.5690	25.6520	0.6550	H	49.5690	25.6520	0.6550
H	53.8420	28.2580	-2.1440	H	53.8420	28.2580	-2.1440
C	54.8670	25.6480	-2.5730	C	54.8670	25.6480	-2.5730
H	55.8815	25.3859	-2.7899	H	55.8815	25.3859	-2.7899
H	54.4906	26.2860	-3.3451	H	54.4906	26.2860	-3.3451
C	49.0840	23.2390	-0.3390	C	49.0840	23.2390	-0.3390
H	48.3495	22.9463	0.3820	H	48.3495	22.9463	0.3820
H	49.1657	22.4831	-1.0919	H	49.1657	22.4831	-1.0919
O	54.7173	21.9014	4.1179	O	54.7173	21.9014	4.1179
H	55.6962	21.9043	4.0821	H	55.6962	21.9043	4.0821
C	44.1360	29.6980	-6.5540	C	44.1360	29.6980	-6.5540
O	43.3730	29.5940	-7.5270	O	43.3730	29.5940	-7.5270
C	42.7200	30.3610	-4.5900	C	42.7200	30.3610	-4.5900
C	42.4300	31.4280	-3.5210	C	42.4300	31.4280	-3.5210
C	42.9810	29.0080	-3.9420	C	42.9810	29.0080	-3.9420
C	43.5690	31.7180	-2.6010	C	43.5690	31.7180	-2.6010
H	41.8380	30.2890	-5.2260	H	41.8380	30.2890	-5.2260
H	42.1690	32.3590	-4.0230	H	42.1690	32.3590	-4.0230
H	41.5940	31.0870	-2.9100	H	41.5940	31.0870	-2.9100
H	43.1990	28.2780	-4.7210	H	43.1990	28.2780	-4.7210
H	43.8310	29.0970	-3.2660	H	43.8310	29.0970	-3.2660
H	42.0940	28.7050	-3.3860	H	42.0940	28.7050	-3.3860
H	43.1740	31.9970	-1.6240	H	43.1740	31.9970	-1.6240
H	44.1890	30.8260	-2.5100	H	44.1890	30.8260	-2.5100

Table S3. (continued)

Table S3. (continued)

H	44.1570	32.5390	-3.0120	H	44.1570	32.5390	-3.0120
N	45.1770	28.8970	-6.3650	N	45.1770	28.8970	-6.3650
C	46.9570	27.3640	-7.0720	C	46.9570	27.3640	-7.0720
H	47.1430	26.5000	-7.7100	H	47.1430	26.5000	-7.7100
H	47.6890	28.1450	-7.2800	H	47.6890	28.1450	-7.2800
H	47.0150	27.0700	-6.0240	H	47.0150	27.0700	-6.0240
H	45.7750	28.9090	-5.5390	H	45.7750	28.9090	-5.5390
C	45.5580	27.9030	-7.3610	C	45.5580	27.9030	-7.3610
H	45.5771	28.3258	-8.3437	H	45.5771	28.3258	-8.3437
H	44.7997	27.1498	-7.3114	H	44.7997	27.1498	-7.3114
C	43.9070	30.7560	-5.4800	C	43.9070	30.7560	-5.4800
H	44.8080	30.8336	-4.9080	H	44.8080	30.8336	-4.9080
H	43.6824	31.7042	-5.9221	H	43.6824	31.7042	-5.9221
C	51.9790	26.1680	-8.1830	C	51.9790	26.1682	-8.1827
S	50.4370	27.0380	-7.9180	S	50.3626	27.0425	-8.0337
H	51.7430	25.2530	-8.7260	H	51.7430	25.2530	-8.7260
H	52.3850	25.9250	-7.2010	H	52.3850	25.9249	-7.2010
C	53.0578	26.9308	-8.9741	C	53.0578	26.9307	-8.9743
H	52.7204	27.9276	-9.1674	H	52.7204	27.9276	-9.1674
H	53.9619	26.9647	-8.4028	H	53.9619	26.9647	-8.4029
H	53.2408	26.4300	-9.9018	H	53.2407	26.4300	-9.9019

Table S4.

Calculated IP values of the CM_H and CM models with and without the environment effect.

	IP(red) values	
	Gas phase	IEFPCM (Eps=4) (7)
CM_H	-1.06	2.59
CM	-3.27	1.62
ΔIP	2.21	0.97

	Distance between the C γ of Asp and the [4Fe-4S] cluster, (Å)	Remarks		Distance(s) between the C δ of Glu and the [4Fe-4S] cluster, (Å)	Remarks
D7	10.5		E9	13.0	
D23	16.6		E45	22.4 21.7	Alternative conformations
D26	12.0		E59	12.8	
D28	11.3		E71	23.4 22.9 22.2	Alternative conformations
D30	13.7		E81	16.4	
D38	16.2				
D39	16.9				
D48	24.0				
D52	19.2				
D53	15.1				
D56	13.7				
D64	10.1				
D70	23.0				
D74	22.4				
D76	18.2				

* Distances are shown by measuring the center-of-gravity coordinates of the [4Fe-4S] cluster and the sidechain terminal carbon of acidic residues.

Table S5.

The distance between the acidic residues and the [4Fe-4S] cluster.*

References

1. Lill R., Broderick J. B., Dean D. R. (2015) **Special issue on iron-sulfur proteins: Structure, function, biogenesis and diseases** *Biochim Biophys Acta* **1853**:1251–1252
2. Matsubara H., Katsube Y., Wada K. (1987) **Iron-sulfur protein research (Japan Scientific Societies Press Tokyo: Springer-Verlag**
3. Pierella Karlusich J. J., Carrillo N. (2017) **Evolution of the acceptor side of photosystem I: ferredoxin, flavodoxin, and ferredoxin-NADP⁺ oxidoreductase** *Photosynth Res* **134**:235–250
4. Valentine R. C. (1964) **Bacterial Ferredoxin** *Bacteriol Rev* **28**:497–517
5. Meyer J. (2008) **Iron-sulfur protein folds, iron-sulfur chemistry, and evolution** *J Biol Inorg Chem* **13**:157–170
6. Beinert H., Holm R. H., Munck E. (1997) **Iron-sulfur clusters: nature's modular, multipurpose structures** *Science* **277**:653–659
7. Hosseinzadeh P., Lu Y. (2016) **Design and fine-tuning redox potentials of metalloproteins involved in electron transfer in bioenergetics** *Biochim Biophys Acta* **1857**:557–581
8. Adman E., Watenpaugh K. D., Jensen L. H. (1975) **NH---S hydrogen bonds in Peptococcus aerogenes ferredoxin, Clostridium pasteurianum rubredoxin, and Chromatium high potential iron protein** *Proc Natl Acad Sci U S A* **72**:4854–4858
9. Dey A., et al. (2007) **Solvent tuning of electrochemical potentials in the active sites of HiPIP versus ferredoxin** *Science* **318**:1464–1468
10. Hirano Y., Takeda K., Miki K. (2016) **Charge-density analysis of an iron-sulfur protein at an ultra-high resolution of 0.48 Å** *Nature* **534**:281–284
11. Hanazono Y., et al. (2022) **Revisiting the concept of peptide bond planarity in an iron-sulfur protein by neutron structure analysis** *Sci Adv* **8**
12. Fukuyama K., Okada T., Kakuta Y., Takahashi Y. (2002) **Atomic resolution structures of oxidized [4Fe-4S] ferredoxin from Bacillus thermoproteolyticus in two crystal forms: systematic distortion of [4Fe-4S] cluster in the protein** *J Mol Biol* **315**:1155–1166
13. Gilli G., Gilli P. (2009) **The Nature of the Hydrogen Bond. Outline of a Comprehensive Hydrogen Bond Theory** Oxford: Oxford University Press
14. Zhou P., Tian F., Lv F., Shang Z. (2009) **Geometric characteristics of hydrogen bonds involving sulfur atoms in proteins** *Proteins* **76**:151–163
15. Kitagawa Y., et al. (2008) **Theoretical studies on effects of hydrogen bonds attaching to cysteine ligands on 4Fe-4S clusters** *Int. J. Quant. Chem* **108**:2881–2887
16. Torres R. A., Lovell T., Noodleman L., Case D. A. (2003) **Density functional and reduction potential calculations of Fe₄S₄ clusters** *J Am Chem Soc* **125**:1923–1936

17. Mouesca J. M., Chen J. L., Noodleman L., Bashford D., Case D. A. (1994) **Density Functional/Poisson-Boltzmann Calculations of Redox Potentials for Iron-Sulfur Clusters** *J. Am. Chem. Soc* **116**:11898–11914
18. Era I., et al. (2021) **Theoretical Study on Redox Potential Control of Iron-Sulfur Cluster by Hydrogen Bonds: A Possibility of Redox Potential Programming** *Molecules* **26**
19. Chen K., et al. (2002) **Azotobacter vinelandii ferredoxin I: a sequence and structure comparison approach to alteration of [4Fe-4S]²⁺/+ reduction potential** *J Biol Chem* **277**:5603–5610
20. Shen B., et al. (1994) **Azotobacter vinelandii ferredoxin I. Alteration of individual surface charges and the [4Fe-4S]²⁺/+ cluster reduction potential** *J Biol Chem* **269**:8564–8575
21. Langen R., Jensen G. M., Jacob U., Stephens P. J., Warshel A. (1992) **Protein control of iron-sulfur cluster redox potentials** *J Biol Chem* **267**:25625–25627
22. Moore G. R., Pettigrew G. W., Rogers N. K. (1986) **Factors influencing redox potentials of electron transfer proteins** *Proc Natl Acad Sci U S A* **83**:4998–4999
23. Chen K., et al. (2002) **Crystal structures of ferredoxin variants exhibiting large changes in [Fe-S] reduction potential** *Nat Struct Biol* **9**:188–192
24. Caspy I., Borovikova-Sheinker A., Klaiman D., Shkolnisky Y., Nelson N. (2020) **The structure of a triple complex of plant photosystem I with ferredoxin and plastocyanin** *Nat Plants* **6**:1300–1305
25. Kubota-Kawai H., et al. (2018) **X-ray structure of an asymmetrical trimeric ferredoxin-photosystem I complex** *Nat Plants* **4**:218–224
26. Kurisu G., et al. (2001) **Structure of the electron transfer complex between ferredoxin and ferredoxin-NADP⁺ reductase** *Nat Struct Biol* **8**:117–121
27. Shirakawa T., et al. (2005) **Identification of variant molecules of Bacillus thermoproteolyticus ferredoxin: crystal structure reveals bound coenzyme A and an unexpected [3Fe-4S] cluster associated with a canonical [4Fe-4S] ligand motif** *Biochemistry* **44**:12402–12410
28. Tokumoto U., Takahashi Y. (2001) **Genetic analysis of the isc operon in Escherichia coli involved in the biogenesis of cellular iron-sulfur proteins** *J Biochem* **130**:63–71
29. Tanaka I., et al. (2010) **Neutron structure analysis using the IBARAKI biological crystal diffractometer (iBIX) at J-PARC. Acta crystallographica. Section D Biological crystallography** **66**:1194–1197
30. Ohhara T., et al. (2009) **Development of data processing software for a new TOF single crystal neutron diffractometer at J-PARC. Nuclear Instruments and Methods in Physics Research Section A: Accelerators, Spectrometers Detectors and Associated Equipment** **600**:195–197
31. Otwinowski Z., Minor W., Carter J. C.W., Sweet R. M. (1997) **Processing of X-ray diffraction data collected in oscillation mode** *Methods in Enzymology* New York: Academic Press :307–326

32. Murshudov G. N., et al. (2011) **REFMAC5 for the refinement of macromolecular crystal structures** *Acta Crystallogr D Biol Crystallogr* **67**:355–367
33. Adams P. D., et al. (2010) **PHENIX: a comprehensive Python-based system for macromolecular structure solution.** *Acta crystallographica. Section D Biological crystallography* **66**:213–221
34. Emsley P., Cowtan K. (2004) **Coot: model-building tools for molecular graphics** *Acta crystallographica. Section D, Biological crystallography* **60**:2126–2132
35. DeLano W. L. (2002) **The PyMOL Molecular Graphics System** San Carlos, CA: DeLano Scientific LLC
36. Frisch M. J., et al. (2009) **Gaussian 09 Rev.C01** Wallingford, CT, USA: Gaussian Inc.
37. Matsui T., Kitagawa Y., Shigeta Y., Okumura M. (2013) **A Density Functional Theory Based Protocol to Compute the Redox Potential of Transition Metal Complex with the Correction of Pseudo-Counterion: General Theory and Applications** *J Chem Theory Comput* **9**:2974–2980
1. Delaglio F., et al. (1995) **NMRPipe: a multidimensional spectral processing system based on UNIX pipes** *J Biomol NMR* **6**:277–293
2. Lee W., Tonelli M., Markley J. L. (2015) **NMRFAM-SPARKY: enhanced software for biomolecular NMR spectroscopy** *Bioinformatics* **31**:1325–1327
3. Sattler M., Schleucher J., Griesinger C. (1999) **Heteronuclear multidimensional NMR experiments for the structure determination of proteins in solution employing pulsed field gradients** *Progress in Nuclear Magnetic Resonance Spectroscopy* **34**:93–158
4. Clowes R. T., Boucher W., Hardman C. H., Domaille P. J., Laue E. D. (1993) **A 4D HCC(CO)NNH experiment for the correlation of aliphatic side-chain and backbone resonances in ¹³C/¹⁵N-labelled proteins** *Journal of Biomolecular NMR* **3**:349–354
5. Kostic M., Pochapsky S. S., Pochapsky T. C. (2002) **Rapid Recycle ¹³C',¹⁵N and ¹³C,¹³C' Heteronuclear and Homonuclear Multiple Quantum Coherence Detection for Resonance Assignments in Paramagnetic Proteins: Example of Ni²⁺-Containing Acireductone Dioxygenase** *Journal of the American Chemical Society* **124**:9054–9055
6. Ying J., Li F., Lee J. H., Bax A. (2014) **¹³Calpha decoupling during direct observation of carbonyl resonances in solution NMR of isotopically enriched proteins** *J Biomol NMR* **60**:15–21
7. Li L., Li C., Zhang Z., Alexov E. (2013) **On the Dielectric “Constant” of Proteins: Smooth Dielectric Function for Macromolecular Modeling and Its Implementation in DelPhi** *J Chem Theory Comput* **9**:2126–2136

Author information

Kei Wada

Department of Medical Sciences, University of Miyazaki, Kiyotake, Japan, Frontier Science Research Center, University of Miyazaki, Kiyotake, Japan
ORCID iD: [0000-0001-7631-4151](https://orcid.org/0000-0001-7631-4151)

For correspondence: keiwada@med.miyazak-u.ac.jp

Kenji Kobayashi[†]

Graduate School of Science and Engineering, Ibaraki University, Hitachi, Japan

[†]These authors contributed equally

Iori Era[†]

Graduate School of Engineering Science, Osaka University, Toyonaka, Japan

[†]These authors contributed equally

Yusuke Isobe

Graduate School of Science and Engineering, Ibaraki University, Hitachi, Japan

Taigo Kamimura

Graduate School of Engineering Science, Osaka University, Toyonaka, Japan

Masaki Marukawa

Department of Medical Sciences, University of Miyazaki, Kiyotake, Japan

Takayuki Nagae

Department of Molecular Biophysics, Tokyo University of Pharmacy and Life Sciences, Tokyo, Japan

Kazuki Honjo

Graduate School of Engineering Science, Osaka University, Toyonaka, Japan

Noriko Kaseda

Department of Medical Sciences, University of Miyazaki, Kiyotake, Japan

Yumiko Motoyama

Department of Medical Sciences, University of Miyazaki, Kiyotake, Japan

Kengo Inoue

Department of Biochemistry and Applied Biosciences, Faculty of Agriculture, University of Miyazaki, Miyazaki, Japan

Masakazu Sugishima

Department of Medical Biochemistry, Kurume University School of Medicine, Kurume, Japan

Katsuhiro Kusaka

Comprehensive Research Organization for Science and Society (CROSS) Neutron Science and Technology Center, Naka Ibaraki, Japan

Naomine Yano

Graduate School of Science, Osaka University, Toyonaka, Japan, Structural Biology Division,
Japan Synchrotron Radiation Research Institute, Hyogo, Japan

Keiichi Fukuyama

Research and Education Center for Atomic Sciences Ibaraki University, Naka Ibaraki, Japan

Masaki Mishima

Department of Molecular Biophysics, Tokyo University of Pharmacy and Life Sciences, Tokyo,
Japan

Yasutaka Kitagawa

Graduate School of Engineering Science, Osaka University, Toyonaka, Japan

For correspondence: kitagawa.yasutaka.es@osaka-u.ac.jp

Masaki Unno

Graduate School of Science and Engineering, Ibaraki University, Hitachi, Japan, Research and
Education Center for Atomic Sciences Ibaraki University, Naka Ibaraki, Japan

For correspondence: masaki.unno.19@vc.ibaraki.ac.jp

Editors

Reviewing Editor

Amy Andreotti

Iowa State University, Ames, United States of America

Senior Editor

Amy Andreotti

Iowa State University, Ames, United States of America

Reviewer #1 (Public review):

Summary:

The authors introduced neutron crystallography coupled with room temperature X-ray crystallography to exam the redox properties of the BtFt [4Fe-4S] cluster expressed in *E. coli*. Neutron structure allowed the authors to exam the influence of Asp64 on the redox properties of the [4Fe-4S] cluster. The neutron structure also allowed for the identification of the hydrogen network around the [4Fe-4S] structure. This work was followed by density functional theory calculation to examine different redox states which also pointed to the role of Asp64 in affecting or dictating redox function of the [4Fe-4S] cluster. Based on the DFT work the authors examine the redox properties under oxic and anoxic conditions in wild type enzymes and in a D64N mutant again showing the role of Asp64 on the redox kinetics and redox potential of the [4Fe-4S] cluster. Lastly, the authors examined similar [4Fe-4S] ferredoxins from several organisms and with a Asp64 or Glu64 observed a similar role of Asp64 on the low potential state of the [4Fe-4S] cluster. The major conclusion of the study was to identify the role of specific amino acids, in this case Asp64, in controlling the redox state and kinetics of [4Fe-4S] clusters. The authors also demonstrate the strength of neutron crystallography when combined with classical X-ray crystallography and classical spectral/redox studies.

Strengths:

In general, the experimental design is logical and the results are convincing demonstrating the role of Asp64 on the redox properties of [4Fe-4S] clusters in ferredoxins.

Weaknesses:

The role(s) of coordinating amino acids on the redox properties of a functional group is not surprising, this reviewer believes this is a novel result in ferredoxins and does make a nice contribution to the field.

<https://doi.org/10.7554/eLife.102506.1.sa1>

Reviewer #2 (Public review):

In this study, Wada et al. investigate the low potential ferredoxin from *Bacillus thermoproteolyticus* (BtFd) using a combination of neutron crystallography, x-ray crystallography, DFT and spectroscopy to determine the influence of hydrogen bonding networks on the redox potential of ferredoxin's 4Fe-4S cluster. The use of neutron diffraction allowed the authors to probe the precise location of hydrogens around the 4Fe-4S cluster, which was not possible from prior studies, even with the previously reported high-resolution (0.92 Å) structure of BtFd. This allowed the authors to revise prior models of the proposed H bonding network theorized from earlier x-ray crystallography studies (for example, showing that there is not in fact a H bond formed between the Thr63-O γ 1 and the [4Fe-4S]-S4 atoms). With this newly described H-bonding network established, the electronic structure of the 4Fe-4S cluster was then investigated using DFT methodology, revealing a startling role of the deprotonated surface residue Asp64, which bears substantial electronic density in the LUMO which is otherwise localized to the 4Fe-4S cluster. While aspartate is usually deprotonated at physiological pH, the authors provide compelling evidence that this aspartate has a much higher pKa than is usual, and is able to act as a protonation-dependent switch which controls the stability of the reduced state of the 4Fe-4S cluster, and thus the redox potential.

The findings of this study and the conclusions drawn from them are well supported by the data and computational work. Their findings have implications for similar control mechanisms in other, non-ferredoxin 4Fe-4S bearing electron transport proteins which have yet to be explored, providing great value to the metalloprotein community. One change that the authors may consider to enhance the clarity of the manuscript regards the nomenclature used for the varying models discussed (CM, CMNA, CMH and so forth). It would be beneficial to the reader if the nomenclature included the redox state (ox. vs red.) of the model in the model's name.

<https://doi.org/10.7554/eLife.102506.1.sa0>